Comet 81P/Wild 2 dust impactors of Stardust turnip-like tracks analogous to cluster IDPs

Mingming Zhang[a*], Noël Chaumard[a†], Céline Defouilloy [a‡], William O. Nachlas[b], Donald E. Brownlee[c], David J. Joswiak[c], Andrew J. Westphal[d], Zack Gainsforth[d], Kouki Kitajima[a], Noriko T. Kita[a]

[a] *WiscSIMS, Department of Geoscience, University of Wisconsin–Madison, Madison, WI 53706, USA*

[b] *Eugene Cameron Electron Microprobe Laboratory, Department of Geoscience, University of Wisconsin–Madison, Madison, WI 53706, USA*

[c] *Department of Astronomy, University of Washington, Seattle, WA 98195, USA*

[d] *Space Sciences Laboratory, University of California, Berkeley, California 94720, USA*

[†]*Present address: Fi Group, Direction scientifique, 14 terrasse Bellini, 92800 Puteaux, France*

[‡] *Present address: CAMECA, 29 quai des Grésillons, 92633 Gennevilliers Cedex, France*

[*]*Corresponding address:* mzhang467@wisc.edu

ABSTRACT

We measured oxygen isotope ratios of 16 silicate fragments from seven aerogel tracks (turnip-like type B tracks 77, 149, 172, 191, and 220; carrot-like type A tracks 22 and 175) of the comet 81P/Wild 2 collector from NASA's Stardust mission using secondary ion mass spectrometry. Thirteen were prepared by ultramicrotomy; three from track 220 were prepared by sputtering resin blocks using a SIMS Kohler beam, a new procedure aiming to mine as many cometary particles encased in aerogel/resin as possible. Combining new and literature results, we recognized that most silicate fragments of individual type B tracks have diverse mineralogy but consistent mass-independent fractionation of oxygen isotopes ($\Delta^{17}O = \delta^{17}O - 0.52 \times \delta^{18}O$) or display negative $\Delta^{17}O$–Mg# relationship like CR chondrules. These observations suggest that their impactors are loosely bound aggregates of unequilibrated materials originating mainly from similar protoplanetary disk regions, resembling the cluster IDP U2-20-GCA. Furthermore, silicate fragments from type A track 22 have almost identical mineralogy and $\Delta^{17}O$ values, confirming that its impactor is a single chondrule-like fragment. The terminal particle of type A track 175 is pure forsterite with $\Delta^{17}O$ of ~–23‰.

Six iron-rich fragments of this study have positive oxygen isotope ratios ($\Delta^{17}O$~+2‰) and ordinary chondrite chondrule-like olivine compositions. Together with five similar fragments in the literature, a unique population (Mg# ≤86) of Wild 2 fragments that resemble chondrules from the inner solar system (O-E-R) chondrites or the outer solar system CH-CB chondrites was identified. The remaining ^{16}O-poor Wild 2 fragments are Mg# ≥79 silicates with $\Delta^{17}O$~–2‰ and a small amount of Mg# ≤79 silicates with $\Delta^{17}O$~0‰, which are most consistent with CR chondrite chondrules. Thus, we conclude

that in addition to the possible major source of CR chondrite chondrule-like materials, the inner solar system or CH-CB chondrule-like materials are a minor component of comet Wild 2, like the cluster IDP U2-20-GCA.

Keywords: silicate fragments; comet Wild 2; inner solar system materials; CR chondrite chondrules; aerogel tracks.

1. Introduction

Thousands of particles from comet 81P/Wild 2 were successfully captured by the silica aerogel collector on the Stardust spacecraft during a 6.1 km/s flyby in 2004 and were returned to Earth for laboratory analysis in 2006 (Brownlee et al., 2006). Two major types of aerogel tracks were identified: (i) carrot-like (type A) tracks, characterized by long, slender, and continuously tapering walls; their impactors are likely single minerals or competent assemblages of a few minerals without adhering fine-grained materials, analog to coarse-grained interplanetary dust particle (IDP) or chondrule fragments; (ii) turnip-like (type B) tracks, characterized by bulbous cavities attached with one or a small number of slender tracks; their impactors are possibly weakly bonded mixtures of unequilibrated coarse- and fine-grained materials, analog to cluster IDP or chondrite matrix (+clast) (e.g., Hörz et al., 2006; Kearsley et al., 2006; Burchell et al., 2008; Joswiak et al., 2012). After extracting individual tracks as keystones from the cometary collector and preparing them by ultramicrotomy (e.g., Westphal et al., 2004; Matrajt and Brownlee, 2006), a significant fraction of high-temperature crystalline silicates (mainly olivine and pyroxene) was identified and found to be similar to chondritic materials, such as chondrules, calcium-aluminum-rich inclusions (CAIs), and amoeboid olivine aggregates (AOAs) (e.g., Zolensky et al., 2006; Nakamura et al., 2008; Simon et al., 2008; Westphal et al., 2009; Nakamura-Messenger et al., 2011; Bridges et al., 2012; Joswiak et al., 2012, 2017; Gainsforth et al., 2015).

Wild 2 olivine fragments exhibit a flat distribution of forsterite contents [mol% Mg/(Fe + Mg), 100 to 52] and a wide range of MnO/FeO ratios, implying diverse sources of carbonaceous (CC, mainly CR and CH) and noncarbonaceous (NC, like ordinary chondrite)

chondrites-forming regions (Frank et al., 2014; Brownlee and Joswiak, 2017). The olivine and pyroxene fragments (N=25, at precision <2-3‰) display a bimodal oxygen isotope distribution that is mostly along the primitive chondrule mineral (PCM) line with mass-independent fractionation of oxygen isotopes, $\Delta^{17}O$ (= $\delta^{17}O - 0.52 \times \delta^{18}O$), ranging from –23‰ to +2‰ (Nakamura et al., 2008; Nakashima et al., 2012; Ogliore et al., 2012, 2015; Gainsforth et al., 2015; Defouilloy et al., 2017). Five fragments of pure forsterite, LIME (low-iron, manganese-enriched) olivine, and enstatite are ^{16}O-rich ($\Delta^{17}O \sim -23‰$), resembling AOAs; the remaining are ^{16}O-poor with those having Mg# [mol% Mg/ (Fe + Mg)] >97 have $\Delta^{17}O \sim -2‰$ and Mg# <97 ones have $\Delta^{17}O$ varying between –4‰ and 2‰ (Nakashima et al., 2012; Defouilloy et al., 2017). This $\Delta^{17}O$–Mg# relationship is most consistent with CR chondrite chondrules, i.e., $\Delta^{17}O$ gradually increases from –6‰ to +1‰ as Mg# decreases from 99 to 94 and then varies between –2‰ to +1‰ in Mg# <90 ones (Connolly and Huss, 2010; Schrader et al., 2013, 2014; Tenner et al., 2015). Furthermore, the ^{26}Al-^{26}Mg analyses of plagioclase/mesostasis-bearing fragments did not detect resolvable ^{26}Mg excess and suggest crystallization ages of >1.7-3.0 Ma after CAI (Matzel et al., 2010; Ogliore et al., 2012; Nakashima et al., 2015), as late as the formation of the majority of chondrules in CR chondrites (Nagashima et al., 2014; Schrader et al., 2017; Tenner et al., 2019).

Cluster IDPs collected from the stratosphere are uncompacted, loosely bonded aggregates composed of coarse monomineralic grains (mainly olivine and low-Ca pyroxene), mineral assemblages (Kool grains, chondrules, AOAs, and CAIs), and chondritic fine-grained materials (enstatite whiskers, organics, presolar grains, and GEMS = glass with embedded metal and sulfide,), representing a heterogeneous breccia physically combined

in the early solar nebula or the regolith of parent comets/asteroids (Thomas et al., 1995; Messenger, 2000; Joswiak et al., 2009, 2017; Ogliore et al., 2019; Zhang et al., 2021; Utt et al., 2023). Their physical and mineralogical characteristics match well with the properties of impactors that produced type B aerogel tracks (e.g., Joswiak et al., 2012), except that the fine materials might have largely been destroyed during the high-speed capture process (Ishii et al., 2008; Floss et al., 2013; Stodolna et al., 2014; Gainsforth et al., 2019). Al-Mg chronology of an amorphous fragment ("Manchanito") from a cluster IDP L2071 indicates a late formation age of >3.2 Ma after CAIs, similar to Wild 2 fragments (Ogliore et al., 2019). The giant cluster (GC) IDP U2-20-GCP (~350 μm in diameter), collected by a U2 aircraft in 1980 as part of the University of Washington high-altitude stratospheric dust collector projects, contains thousands of submicron to ~40 μm particles with extreme diverse mineralogy (Joswiak et al., 2017). Its iron-rich olivine displays wide ranges of Fe and Mn contents, indicating diverse sources of various chondrule-forming environments, resembling Wild 2 fragments (Brownlee and Joswiak, 2017). Oxygen isotope systematics of 20 silicate fragments (mono/polymineralic olivine and pyroxene, and chondrule-like fragments) from this cluster IDP show limited oxygen isotope range with $\Delta^{17}O$ increasing from –3‰ to 0‰ with decreasing Mg# (99 to 75), comparable to Wild 2 fragments and CR chondrule-like materials; minor fragments have positive oxygen isotope ratios that were likely derived from NC-like or CH-CB chondrule-like materials (Zhang et al., 2021). The oxygen isotope study demonstrated that most silicate fragments in cluster IDPs could be derived from similar protoplanetary disk regions where they aggregated as clusters before being transported to and then accreted into parental comets.

Since there are many similarities between Wild 2 fragments and cluster IDPs, we studied the mineralogy and oxygen isotopes of 16 large (>2 μm) silicate fragments from seven Stardust aerogel tracks to explore the potential genetic relationships between the dust impactors of aerogel tracks and cluster IDPs, and further constrain the source of Wild 2 silicates. In addition to the conventional ultramicrotomy method, we developed an analytical procedure of exposing the fully embedded Wild 2 fragments in the subsurface of acrylic/epoxy resin blocks using the Kohler beam of secondary ion mass spectrometry (SIMS). The procedure aims to mine as many silicate fragments embedded in the resin during sample preparation as possible, which is typical for fragment clusters in the bulb regions of type B tracks.

2. Analytical Methods

2.1 Sample descriptions and preparation

Silicate fragments from seven aerogel tracks were investigated in this study, including additional fragments from five tracks (T22, T77, T149, T172, and T191) that have been previously studied (Joswiak et al., 2012; Nakashima et al., 2012; Defouilloy et al., 2017; Gainsforth et al., 2019), and new fragments from two tracks (T175 and T220) that have been recently extracted. Five (T77, T149, T172, T191, and T220) are type B tracks. T77 (named "Puki") is a >1.2 mm-long track containing >54 discrete fragments distributed throughout the bulb region, along the main track, and in the three short sidetracks (Joswiak et al., 2012). T149 is a ~4 mm-long track composed of the main track, two short sidetracks, and a broad cavity (Defouilloy et al., 2017). T172 is a ~0.9 mm-long track with a distinct narrow root (Defouilloy et al., 2017). T191 is a ~11 mm-long track whose terminal particle is a large pyrrhotite crystal associated with fine-grained materials of equilibrated

aggregates, possible GEMS, and altered objects (named "Andromeda" as a whole) (Gainsforth et al., 2019). T220 is a ~5.3 mm-long track consisting of at least six terminal particles, numerous small particles within the bulb, and large areas of melt. Tracks 22 and 175 are type A with a length of ~3.9 mm and ~1.3 mm, respectively. T22 (named "Aton") contains at least five visible short sidetracks extending off the main branch (Joswiak et al., 2012).

Aerogel keystones containing entire tracks were prepared at the University of California, Berkeley (UCB) or the Johnson Space Center curatorial facility (Westphal et al., 2004). Keystones of T22, T77, T149, T172, and T175 were compressed and embedded into acrylic resin at the University of Washington following the procedure described in Matrajt and Brownlee (2006). The acrylic resin was cut into individual slabs based on the distribution of large (>2 μm, suitable for SIMS oxygen isotope analysis) transparent fragments (mainly crystalline silicates). Each acrylic slab was then glued on top of an acrylic cylinder with 7 mm diameter and 10 mm height and trimmed for ultramicrotomy. The T191 keystone was embedded in an EMBED 812 epoxy bullet for ultramicrotomy at the UCB, as described in Gainsforth et al. (2019). The T220 keystone was processed at both institutions as part of a consortium study. ~70-100 nm-thick microtome sections of silicate fragments were made by ultramicrotomy. These sections were transferred onto commercially prepared 200-mesh Cu or Au TEM grids coated with 10 nm-thick carbon films for transmission electron microscope (TEM) observations (Joswiak et al., 2009, 2012; Gainsforth et al., 2015, 2019). The remaining portion ("potted butt") was removed from the acrylic cylinder or epoxy bullet and pressed into 1.4 mm diameter indium metal located at the center of a 25 mm or 8 mm aluminum disk for SIMS analysis (Nakashima et al., 2012;

Defouilloy et al., 2017; Zhang et al., 2021). A polished San Carlos olivine (SC-Ol) grain used as a SIMS running standard was pressed within 500 μm of the potted butt.

The ultramicrotomy method exposes the upmost-level fragment(s) of the resin block for mining the terminal particles and other fragments dispersed in most aerogel tracks of this study. However, for track 220 which has clustered fragments in its bulb region at different depths in resin blocks, ultramicrotomy cannot separate and expose them individually. In this case, we developed an analytical procedure of exposing subsurface fragments by SIMS Kohler beam sputtering the resin blocks, followed by Electron Probe Micro-Analyzer (EPMA) major element measurement and SIMS oxygen isotope analysis (section 2.3).

2.2 Analytical procedures for Wild 2 fragments exposed by ultramicrotomy

The Wild 2 fragments exposed by ultramicrotomy were analyzed following the procedure described in Nakashima et al. (2012), Defouilloy et al. (2017), and Zhang et al. (2021). They were first imaged with field-emission-gun (FEG) scanning electron microscopes (FEG-SEMs; JEOL JSM 7000F at the University of Washington; Zeiss Auriga and Zeiss Gemini 450 at the University of Wisconsin-Madison, UW-Madison) and a conventional tungsten-sourced SEM (Hitachi S3400, UW-Madison). Images were taken with low beam currents (≤ 200 pA) for a short acquisition time (<30 s). Under this condition, the electron beam damage and shrinkage of resins were minor (<0.2 μm depression), as inspected by a Zygo NewView™ 9000 interferometer at the Nanoscale Imaging and Analysis Center (NIAC), UW-Madison. Their mineral chemistries were determined from their microtome sections using a FEG transmission electron microscope (Tecnai TF20 STEM, 200 keV) at the

University of Washington, following the method described in Joswiak et al. (2009). Quantitative energy dispersive X-ray (EDX) spectra were obtained using a light element X-ray detector and quantified using an EDAX Genesis analysis system by the k-factor element ratio technique (Cliff and Lorimer, 1975). Typical detection limits were ~0.01 wt%. Estimated relative errors are <5% for major elements and ~30% for minor elements.

Before SIMS analysis, the Wild 2 fragments were marked by removing 1 × 1 μm square(s) of carbon coating (20-30 nm thick) on the sample surface using a focused ion beam (FIB) SEM (Zeiss Auriga) at NIAC, UW-Madison. The Ga^+ FIB with an acceleration voltage of 30 keV and a beam current of 5 pA was used to sputter target regions for 90 s, which was proven to be effective for removing this thickness of carbon coating with minimal alteration of the underlying samples (Nakashima et al., 2012; Defouilloy et al., 2017; Zhang et al., 2021).

The oxygen isotope ratios of Wild 2 fragments were determined using the CAMECA IMS-1280 at the WiscSIMS laboratory of UW-Madison. Three sessions of similar analytical conditions were performed (Feb. 2017, Oct. 2017, and Oct. 2021), with the first two also analyzing silicate fragments from the cluster IDP U2-20-GCA (Zhang et al., 2021). A typical primary Cs^+ beam with a size of ~ 2 × 1.5 μm and an intensity of 2.5-3 pA was used. A normal incident electron gun (NEG) was used for charge compensation. Precise aiming of target locations was enabled by the FIB marks, which appeared as bright spots on a $^{16}O^-$ ion image generated by rastering the primary beam over a 10×10 μm square of the nearest region (Nakashima et al., 2012), and the "Nanodeflector," which can deflect the primary beam by ≥0.1 μm steps (Defouilloy et al., 2017). Secondary ions $^{16}O^-$ (2-3×10^6 cps = counts per second), $^{17}O^-$, and $^{18}O^-$ were detected simultaneously using a Faraday cup with an

amplifier of 10^{11} Ω resistance and two electron amplifiers (EMs) on the multicollection system, respectively. The contribution of $^{16}O^{1}H^{-}$ tailing on the counts of $^{17}O^{-}$ was ≤20 ppm under a mass resolving power (MRP) of ~6000 at mass 17, which was corrected using the $^{16}O^{1}H^{-}$ intensity monitored at the end of each analysis following the method described in Heck et al. (2010). Each measurement took ~25 min that included 20 cycles of acquisition of 60 s each, with typical internal uncertainty (2SE) of 1.5 ‰, 2.0 ‰, and 2.0 ‰ for $\delta^{18}O$, $\delta^{17}O$, and $\Delta^{17}O$, respectively. The uncertainty assigned to the unknowns is represented by twice the standard deviation (2SD) of the bracketing six analyses on the SC-Ol of the same disk (Kita et al., 2009), which is similar to the 2SE of individual analysis. The instrumental biases of unknown analysis were estimated from the multiple matrix-matching olivine and pyroxene standards analyzed in the same SIMS sessions (Table S1). The locations and morphology of SIMS pits on Wild 2 fragments were inspected using the SEMs Zeiss Auriga and Hitachi S3400 mentioned above (Supplementary material 4).

2.3 Analytical procedures for subsurface Wild 2 fragments in resin blocks

2.3.1 Expose silicate fragments using SIMS Kohler beam

Subsurface Wild 2 fragments (associated with a small amount of silica aerogel) in two acrylic resin blocks of T220 were first located by the navigational QGIS program, where the transmitted (taken before embedding into the indium metal of an aluminum disk) and reflected light microscope images of the resin blocks were aligned with the sample stage using the coordinates of reference points. Then, the in-house QGIS plugins enable the operation of the SIMS XY stage in the QGIS program with an accuracy of 2 μm (Linzmeier et al., 2018). The aiming accuracy would be confirmed by live images of the UV light-

illuminated microscope camera (optical resolution ~1.3 μm) (Kita et al., 2015), where the exposed fragments could be readily identified from the substrate.

Hereafter, they were exposed using a SIMS Cs^+ primary beam under the Kohler illumination mode ("Kohler beam"), which provides relatively fast and homogeneous sputtering. The primary ion beam was tuned to be ~22 × 22 μm (near circle) using a beam aperture of 100 μm in diameter (a larger aperture produces a larger beam). The beam intensity was adjusted to be 0.5-1.0 nA, and the field aperture was set to 6000 μm. Charge compensation was achieved using a NEG. Secondary ion of major oxides in olivine and pyroxene, i.e., $^{18}O^-$, $^{24}Mg^{16}O^-$,$^{27}Al^{16}O^-$, $^{28}Si^-$, $^{40}Ca^-$, $^{52}Cr^-$, $^{55}Mn^-$, and $^{56}Fe^-$, were counted using a Faraday cup and an EM on the monocollection (mono-) system under peak-jumping mode. The MRP was set to be ~5000 to separate interferences of $^{28}Si^{28}Si^-$ on $^{56}Fe^-$. Each cycle took ~38 s, and cycle-by-cycle count rates for each ion species were monitored. Depending on the mineral species, the count rates of some ion species (except for ^{28}Si–, signals also generated from silica aerogel) would dramatically increase if reaching the subsurface silicate fragments. To evaluate the exposed size, a focused (gaussian) beam of ~1 μm in diameter (~7-8 pA) was used to generate ion images over a 10 × 10 μm square using the monoEM. We repeatedly switched between the Kohler and Gaussian beam conditions until the silicate fragment was almost fully exposed or the exposed area was roughly >2×2 μm. Zhang et al. (2022) found that the SIMS sputter rates of epoxy (~0.88 μm^3/s/nA) and acrylic resins (~1.03 μm^3/s/nA) are significantly faster than olivine and pyroxene (0.26-0.43 μm^3/s/nA). Thus, it was never required to expose the maximum dimension of the subsurface silicate fragment, making it stand out from the substrate resin and increasing the possibility of sample charging under NEG. Furthermore, because of the incident angle of

253 the primary beam (~21°) column, we limited the depth to 6 μm for a ~22 μm Kohler beam
254 to minimize the shadow effect of the crater wall.

255 After being exposed by Kohler beam sputtering, the Wild 2 fragments were recoated
256 with ~20 nm carbon. If no coating was applied, the built-up charge around the analysis
257 location would reduce the secondary ion yield (defined as the secondary ion count
258 rate/primary ion intensity) by ~50% and induce significant mass-dependent fractionation
259 of oxygen isotopes during a Gaussian-beam analysis. For example, we found the $\delta^{18}O_{Raw}$ and
260 $\delta^{17}O_{Raw}$ values determined by a Gaussian beam from the bottom of craters made by Kohler
261 beam sputtering on SC-Ol are constantly 9-10‰ higher than those from the polished
262 surface; in contrast, their $\Delta^{17}O_{Raw}$ values are indistinguishable and independent of the
263 crater depth (Fig. 1a-b, Supplementary material 1, Table S2). If a new coating was applied,
264 the measured $\delta^{18}O_{Raw}$ and $\delta^{17}O_{Raw}$ values from the crater bottom and polished surface were
265 almost identical (Fig. 1c-d).

266 ***2.3.2 Major element analysis using EPMA at very low beam current***

267 A FEG-EPMA (CAMECA SX-Five FE) equipped with a horizontal silicon drift energy
268 dispersive spectroscopy detector (EDS) and five wavelength-dispersive spectrometers
269 (WDS) at the Eugene Cameron Electron Microprobe Laboratory, UW-Madison, was used for
270 determining the major and minor element compositions of the exposed fragments. To
271 avoid shifting of beam spot location when switching beam apertures, we used the same
272 electron beam setting for point analysis and scanning, which is necessary to precisely
273 locate the μm-sized Wild 2 fragments at the crater bottoms. Thus, an optimal beam setting
274 must be selected to balance the high-quality quantitative analysis and electron beam
275 damage to the surrounding resin or aerogel. After tests to investigate beam damage and

count rates, it was determined that the optimal beam conditions included a 500 pA beam current, an accelerating voltage of 12 kV, and a beam diameter of 1 μm (set by the software). Each element was measured for 200 s and background subtraction was performed using the Mean Atomic Number (MAN) technique (Donovan et al., 2016). The elements were calibrated using natural standards of Springwater olivine (USNM 2566) (Mg), wollastonite (Ca), jadeite (Na), microcline (K), and synthetic standards of MgO (Mg), Al_2O_3 (Al), Cr_2O_3 (Cr), TiO_2 (Ti), $MnSiO_4$ (Mn), and Fe_2SiO_4 (Si). Typical detection limits were 0.01 wt% for MgO, 0.02 wt% for Na_2O, Al_2O_3, SiO_2, and Cr_2O_3, 0.04 wt% for CaO, 0.05 wt% for TiO_2, and 0.08 wt% for FeO and MnO.

The interaction volume (energy >10%) simulated by the CASINO software (Demers et al., 2011) is ~1.2 (X) × 1.2 (Y) × 2.0 (Z) μm. Under the selected beam conditions, the electron beam damage on the acrylic resin was <0.4 μm deep after ~10 s of test scanning (the time needed for locating analysis positions was considerably shorter than this) and no damage was observed to the C coating. The measured Fo mol% values in olivine reference materials (RMs) and En mol% and Wo mol% values in pyroxene RMs are consistent with their reference values (Fig. 2; EA3; Fukuda et al., 2020; Zhang et al., 2022). Relative standard deviations (RSD) are typically <5% for major elements (>1 wt%), <10% for Cr_2O_3 (>0.4 wt%), and <20% for Al_2O_3 (>0.6 wt%). The MnO contents in olivine and pyroxene RMs measured under these conditions were systematically higher than their reference values but follow a linear trend. The overestimation of MnO content may be related to (i) the low acceleration voltage used, which is less than twice the Mn Kα absorption edge (6.54 kV), and (ii) the low beam current at which measurement were performed, which can be affected by non-linearity in the accuracy of picoammeter measurements that are especially

problematic at very low count rates (Donovan et al., 2023). The MnO contents were corrected using the empirical functions fitting from these olivine and pyroxene RMs (Figs. 2b and 2d).

2.3.3 *SIMS oxygen isotope analysis*

The oxygen isotopes of the exposed T220 fragments were determined using a 1.5 × 1.0 μm-sized primary ion beam with an intensity of ~1.5 pA. The other settings were identical to those used for the 2.0 × 1.5 μm beam described in section 2.2. The typical count rate for $^{16}O^-$ was 1.5-2.0 × 10^6 cps (~60% of that under 2.0 × 1.5 μm beam). The spot-to-spot reproducibility (2SD) on SC-Ol was 1-3‰ for $\delta^{18}O$ and 2-3‰ for $\delta^{17}O$ and $\Delta^{17}O$.

2.3.4 Evaluation of the analytical procedure using a simulant mount

Before applying the analytical procedure to the actual Wild 2 samples, a simulant epoxy mount (without silica aerogel) of augite standard "7244-Aug" (Zhang et al., 2022) powders (10s to 100s of μm-sized fragments) was prepared to evaluate its reliability. Micrometer-sized fragments within 6 μm below the surface were searched under an optical microscope, and six (3-10 μm) were selected for Kohler beam sputtering (Supplementary material 3). Depending on the shape and burial condition of these fragments, their exposed surfaces are highly variable. Two are tilted shards, and the other four are flat plates, as inspected using the Zygo interferometer and an SEM. EPMA analysis on the tilted fragment A3-R1 (~2 × 1 μm, 3.4 μm deep) shows major element compositions consistent with the reference values (RSD<10%, Supplementary material 2). Oxygen isotope analyses on the four flat fragments using a Gaussian beam of 2 × 1.5 μm^2 show similar oxygen isotope ratios to the nearby large grains on the polished surface (Table S4), except for two analyses that could have experienced slight arcing due to thin coatings (SEM imaged multiple times).

3. Results

3.1 Wild 2 fragments exposed by ultramicrotomy

3.1.1 Mineralogy

Thirteen fragments ranging in size from 2 × 2 μm to 7 × 2 μm were extracted from the seven aerogel tracks and prepared by ultramicrotomy (Table 1, Fig. 3). Nine are monomineralic, of which four are iron-rich olivines (T77/F7, T149/F11a, F11b, and T191/B1/F6; Mg# = 60-85), two are magnesian olivines (T191/B1/F2, F3; Mg#~98), one is near pure forsterite (T175/F1, $Fo_{99.8,}$ ~0.1 wt% MnO, not LIME), and two are low-Ca pyroxenes (T172/F100 and T191/B1/F1; $En_{94\text{-}96}Wo_{1\text{-}3}$). T220/TP10b/F10 is polymineralic fragment dominated by low-Ca pyroxene ($En_{95}Wo_{3.4}$) with an Mn-rich olivine (Fo_{87}, ~2.5 wt% MnO) inclusion. T22/F7, F8, and F12 are chondrule-like, dominated by chemically zoned olivine ($Fo_{67\text{-}92}$) with minor silicate glass, like the TP ($Fo_{64\text{-}91}$) and F7 ($Fo_{67\text{-}91}$) of this track (Tomeoka et al., 2008; Joswiak et al., 2012).

Olivine contains minor amounts of MnO (0.1-0.7 wt%), Cr_2O_3 (≤0.8 wt%), Al_2O_3 (<0.6 wt%), and CaO (≤0.4 wt%). On the diagram of Fe (afu) vs. Mn (afu) in olivine (Fig. 4), T22/F8, F12 fall into the "forbidden triangle" that is unique to olivines in Wild 2, anhydrous IDPs, and OC chondrules (Brownlee and Joswiak, 2017; Zhang et al., 2021; Schrader and Davidson, 2022); other iron-rich olivines (except for the Mn-rich olivine inclusion in T220/TP10b/F10) plot close to the trendline of OC chondrules and also within the range of CR chondrules; and magnesian olivine fragments (T191/B1/F2, F3, and T175/F1) have low MnO content (0.1-0.3 wt%) like typical iron-poor chondrules. Furthermore, the three low-Ca pyroxene fragments contain up to 2.9 wt% Al_2O_3 (T220/TP10a/F10), 0.2-1.2 wt% Cr_2O_3, and 0.6-1.3 wt% MnO.

3.1.2 Oxygen isotopes

The thirteen fragments were analyzed only once each due to their small sizes (Table 2, Supplementary Material 4, Table S5). Three analyses penetrated thin fragments T22/F12, T77/F7, and T191B1/F6, and their oxygen isotope ratios were recalculated from ratios of cycles prior to contact with the underlying aerogel or resin beneath (identified by an abrupt decrease in the $^{16}O^-$ signal intensity), without applying the correction of $^{16}O^1H^-$ to $^{17}O^-$. The pure forsterite fragment T175/F1 is ^{16}O-rich ($\delta^{18,17}O \sim -50‰$, Fig. 5a), like AOAs and Wild 2 LIME olivines (Nakashima et al., 2012; Ushikubo et al., 2017; Marrocchi et al., 2019; Fukuda et al., 2021). The remaining fragments are ^{16}O-poor with $\delta^{18}O$, $\delta^{17}O$, and $\Delta^{17}O$ ranging from –3.1 ± 1.7‰ to 6.9 ± 2.4‰, –5.9 ± 3.3‰ to 6.7 ± 4.0‰, and –4.3 ± 2.9‰ to 3.1 ± 2.9‰, respectively (Table 2, Fig. 5b), greatly overlapping with the ^{16}O-poor Wild 2 fragments in the literature (Nakamura et al., 2008; Nakashima et al., 2012; Ogliore et al., 2012, 2015; Gainsforth et al., 2015; Defouilloy et al., 2017).

Unlike most fragments that are distributed on or close to the PCM line, five (F22/F8, F10, and F12, T77/F7, and T191/B1/F6) are plotted on/above the terrestrial fractionation (TF) line (Fig. 5c), including the three that were penetrated during analysis. For the three (F8, F10, and F12) fragments analyzed in track 22, they have indistinguishable $\Delta^{17}O$ values (2.4 ± 1.9‰ to 3.2 ± 2.9‰), while F10 (1.6 ± 1.9‰) has a lower $\delta^{18}O$ compared to the other two (6.9 ± 2.4‰ for F8 and 5.5 ± 2.0‰ for F12, Fig. 5c). For the four fragments analyzed in track 191, three (F1, F2, and F3) have almost identical $\Delta^{17}O$ (~–2‰) and $\delta^{18}O$ (~–2‰), while F6 has significantly positive $\Delta^{17}O$ and $\delta^{18}O$ of 1.8 ± 2.5‰ and 4.7 ± 1.7‰, respectively (Table 2).

3.2 Wild 2 fragments exposed by SIMS Kohler beam sputtering

3.2.1 Mineralogy

Five fragments (TP10a/F3, F4, and F5; TP10b/F11 and F12) with an estimated size of ~2-3 μm and depth of 2-8 μm within the two acrylic blocks (TP10a and TP10b) of track 220 were exposed by SIMS Kohler beam sputtering. After being exposed, SEM and profilometer inspections determined their sizes to be 1.8 × 1.8 μm to 3.0 × 2.3 μm and depths to be 2.3 μm to 7.8 μm (Fig. 6). EPMA analyses identified an iron-rich olivine (Fo_{68}, TP10a/F3) with ~0.52 wt% MnO, plotted close to the OC chondrule trendline in the Fe vs. Mn diagram (Fig, 4). The other four are low-Ca pyroxene ($En_{80\text{-}96}Wo_{1.2\text{-}5}$) containing varying amounts of Al_2O_3 (0.4-4.0 wt%), Cr_2O_3 (0.6-1.3 wt%), and MnO (0.5-1.6 wt%), with those from the same acrylic block having similar compositions ($En_{94\text{-}96}Wo_{1.5\text{-}3}$ for TP10a/ F4 and F5; $En_{80\text{-}84}Wo_{1.2}$-5 for TP10b/F11 and F12). The EPMA analysis total for TP10a/F5 is lower than others (~74 wt% vs. 88-96 wt%) because it is hollow, as revealed during FIB marking (Table 1, Supplementary material 4).

3.3.2 Oxygen isotopes

Except for TP10a/F5, the remaining four exposed fragments were measured for oxygen isotopes, of which TP10b/F12 was penetrated within five analysis cycles (data discarded). The valid analyses on TP10a/F3, F4 and TP10b/F11 show ^{16}O-poor signatures, with $\delta^{18}O$ of 2.9 ± 1.6‰, 4.7 ± 1.6‰, and 2.7 ± 2.8‰, and $\Delta^{17}O$ of 1.6 ± 2.7‰, –1.3 ± 2.7‰, and –2.4 ± 3.1‰, respectively. TP10b/F3 (Fo_{68}) has oxygen isotope ratios plotted on/above the TF line, like the other five fragments mentioned in section 3.1.2 (Fig. 5c). TP10b/F11 shows similar oxygen isotopes to TP10b/F10 ($\delta^{18}O$: 3.5 ± 0.8‰; $\Delta^{17}O$: –1.3 ± 1.7‰), a grain exposed by ultramicrotomy on the same acrylic block.

4. Discussion

4.1 Mining techniques for silicate fragments in aerogel tracks

Ultramicrotomy has been proven to be a very reliable technique for exposing Wild 2 fragments at the track roots or dispersed along the main track, sidetracks, or within its bulbous region (Westphal et al., 2004; Matrajt and Brownlee, 2006; Zolensky et al., 2006; Nakamura-Messenger et al., 2011). However, with numerous fragments dispersed at different depths within the acrylic/epoxy resin, ultramicrotomy only exposes the fragment(s) located at the upmost levels and leaves the others embedded. In this study, we developed a three-step analytical procedure for mining subsurface Wild 2 fragments in acrylic/epoxy resin blocks. Step I: Expose fragments using a SIMS Kohler beam and monitor the sputtering process via the count rate change of major element ions. Step II: Apply a new carbon coating and determine their major and minor element compositions using a 500-pA electron beam on an FE-EPMA. Step III: Determine their oxygen isotope ratios using a SIMS with a primary ion beam size of 1.5 × 1.0 μm or 2.0 × 1.5 μm (if ≥3 μm), with aiming guided by FIB marks. The procedure was set up through parallel tests on an SC-Ol grain and the simulant mount of 7244-Aug, which has been successfully applied to silicate fragments embedded in the two acrylic blocks of track 220.

The procedure has three merits: (i) the mineral species of each fragment and its chemical composition can be well characterized. Melted aerogel associated with fine-grained Mg-/Fe-bearing phase can be easily distinguished and avoided; (ii) oxygen isotope ratios of each fragment can be determined with significantly improved precision (2-3‰ levels); and (iii) the instrumental bias of target fragments can be properly corrected by standards with matching compositions since there is no instrumental bias difference

between fragments on the surface and those several μm below the surface after applying a new carbon coating. Additionally, the spot-to-spot reproducibility of the instrument can be monitored by the nearby running standard, SC-Ol, on the polished surface. However, this procedure has two obvious limitations. First, the exposed area of a fragment (preferably flat) is highly dependent on its shape and orientation in the acrylic/epoxy resin. Only the top surface could be exposed for further analyses due to the differential sputtering rates between silicates and resin. Second, the maximum depth of target fragments is limited by the SIMS Kohler beam size, i.e., ~6 μm for ~22 ×22 μm, due to the shadow effect of the beam crater (~21° inclination angle of the primary ion column). Still, we believe this procedure could greatly improve the efficiency of mining Wild 2 fragments in aerogel tracks supplementary to traditional ultramicrotomy techniques and is particularly useful for small grains.

Ogliore et al. (2015) studied fine-grained materials in the bulb of track 74 by (i) extracting a 1 mm^2 section from the wall of this track using glass needles and then compressing it into indium; (ii) mounting it into an Au-coated Si_3N_4 window with a ~400 μm ion-milled hole; (iii) mapping major elements using an EPMA and then (iv) mapping oxygen isotopes and other ion species of major elements by SIMS using a ~500 nm primary ion beam, and then calculating the oxygen isotope ratios of Mg-Al, or Fe-rich regions (assumed to be fine-grained silicate fragments, typically 1-3 μm). This procedure efficiently obtained the chemistry and oxygen isotope information of tens to hundreds of potential silicate fragments down to 1 μm in size within a single SIMS session. However, compared to the EPMA and SIMS point analyses employed in the procedure developed in this study, ion

imaging cannot reliability determine the mineral species and compositions, nor can it determine the oxygen isotope ratios at high precision (2-3‰ levels).

4.2 Impactor properties of aerogel tracks

Based on the wide ranges of chemical compositions (Mg#: 100 to 60) and oxygen isotope ratios (~–23‰ to ~+1‰) of six fragments, Nakashima et al. (2012) suggested that the impactor of the type B track 77 is an aggregate of silicate fragments formed in environments of refractory inclusions and outer solar system chondrules. For T77/F7 (olivine, Fo_{60}, $\Delta^{17}O$ = 3.0 ± 2.5‰, $\delta^{18}O$= 5.1 ± 1.8‰) analyzed in this study, we found its oxygen isotope ratios are similar to other iron-rich fragments (T77/F1, F4, and F5, Mg#= 60-78, $\Delta^{17}O$~–2‰ to ~2‰, $\delta^{18}O$~6-7‰; Nakashima et al., 2012), but are more ^{16}O-poor than those magnesian-rich ones of the same track (T77/F9, Mg#=96, $\Delta^{17}O$~–3‰;, $\delta^{18}O$~0‰, Nakashima et al., 2012; the "butterfly," Mg#=88, $\Delta^{17}O$~–3‰, $\delta^{18}O$~–6‰, Ogliore et al., 2015) . This increase of $\Delta^{17}O$ with decreasing Mg# appears to be consistent with CR chondrules (Tenner et al., 2015), but T77/F7 and the other three iron-rich fragments plot on/above the TF line and overlap with inner solar system O-E-R chondrules or porphyritic chondrules in CH-CB chondrites, suggesting they are genetically related (Figs. 7a, b). Their possible inner solar system origin is supported by their OC chondrule-like Fe-Mn systematics (Fig. 4). Thus, we confirmed that the dust impactor of T77 is composed of silicate fragments formed in multiple regions, i.e., refractory inclusions, CR chondrules, and O-E-R chondrules or CH/CB chondrules.

To explore whether the impactor properties of T77 can be generalized to all type B tracks, we compiled the oxygen isotopes of silicate fragments from other five type B tracks determined in this study and the literature (Table S6). For tracks 191 and 220 (Figs. 7c, d),

458 we found that Mg# >88 fragments have nearly constant $\Delta^{17}O$ of –2‰. T191/F2 and F3
459 ($Fo_{\sim 98}$, $\Delta^{17}O \sim -2‰$), as well as T220/TP10b/F10 and F11 ($En_{95}Wo_3$, $\Delta^{17}O \sim -2‰$), have
460 almost identical mineralogy and $\Delta^{17}O$ values that likely be parts of single large grains that
461 fragmented during aerogel capture. On the other hand, the two iron-rich ones
462 (T191/B1/F3 and T220/TP10a/F3, Mg# = 75 and 68) have similar $\Delta^{17}O$ of ~2‰ with $\delta^{18,}$
463 ^{17}O plotting on/above the TF line. Their Fe-Mn contents are plotted close to the OC
464 chondrule trend line (Fig. 4). Thus, the two fragments could also be derived from regions
465 like O-E-R chondrules or CH/CB chondrules.

466 For the seven fragments analyzed in track149 (Figs. 7e, f), an enstatite fragment (F2,
467 Mg# = 99.5, $\Delta^{17}O \sim -7‰$) displays more ^{16}O-rich signatures compared to the remaining
468 fragments (F1, F3, F6, F7, F11a, and F11b, Mg#=98-85, $\Delta^{17}O \sim -2‰$ to 1‰; Defouilloy et al.,
469 2017 and this study), similar to chondrules in CR chondrites (Connolly and Huss, 2010;
470 Schrader et al., 2013, 2014; Tenner et al., 2015). Among them, relatively large (~20 μm)
471 fragment T149/F1 and two other small fragments T149/F11a and F11b have almost
472 identical mineralogy (olivine, Mg# ~85) and $\Delta^{17}O$ values ($\Delta^{17}O \sim 0‰$), which are likely
473 parts of a single large grain that fragmented during aerogel capture. For tracks 108 and 74
474 (Figs. 7g, h), "Gozen-sama" and "Gen-chan" from T108 have different mineralogy (olivine +
475 low-Ca pyroxene vs. low-Ca pyroxene + high-Ca pyroxene + glass; Mg#=95 vs. 96), "Iris"
476 and "Calie" from T74 have different $\delta^{18}O$ values (~6‰ vs. ~2‰; Mg#=64), but their $\Delta^{17}O$
477 values are almost identical (~–2‰ and ~0‰, respectively) (Nakamura et al., 2008;
478 Ogliore et al., 2012, 2015; Gainsforth et al., 2015). Thus, we conclude that, except for minor
479 fragments showing oxygen isotopes and Fe-Mn systematics of O-E-R chondrules or CH-CB
480 chondrules, most fragments within individual type B tracks have similar $\Delta^{17}O$ values or

481 display negative $\Delta^{17}O$-Mg# correlation like CR chondrules, suggesting that they could be
482 derived from similar regions of the protoplanetary disk. These fragments of similar origins
483 could show different mineralogy (including Mg#) and/or $\delta^{18,17}O$ values, indicating that
484 they are not from equilibrated parent bodies. These characteristics for impactors of type B
485 tracks are comparable to the silicate fragments in the giant cluster IDP U2-20 GCA (Figs. 7 k,
486 l), displaying complex mineralogy (Mg# = 99-75) and variable $\delta^{18,17}O$ (~–6‰ to 6‰) but
487 a small range of $\Delta^{17}O$ (~–3‰ to 3‰) that suggest a major source of CR chondrule-like
488 materials and a minor source of the inner solar system/CH-CB chondrule-like materials
489 (Brownlee and Joswiak, 2017; Zhang et al., 2021). Therefore, the impactors of type B tracks
490 are analogous to cluster IDPs.

491 In contrast to type B tracks, a comprehensive mineralogy study of multiple type A
492 tracks indicated that their impactors were composed of single mineral grains, possible
493 chondrule fragments, and other polymineralic assemblages (Joswiak et al., 2012). The track
494 22 is unusual type A track having multiple relatively coarse fragments (Joswiak et al., 2012),
495 which gave us an opportunity to test the nature of the impactor from oxygen 3-isotope
496 analyses. Three fragments T22/F8, F10, and F12 f analyzed in this study are type II
497 chondrule-like materials composed of unequilibrated olivine (Fo_{67-93}) and silicate glass,
498 also identical to the terminal particle F1 and fragment F7 previously studied in the same
499 track (Tomeoka et al., 2008; Joswiak et al., 2012). The analyses of three fragments from this
500 study and one of the two analyses in F7 (Nakashima et al., 2012) show indistinguishable
501 positive $\Delta^{17}O$ values (~2‰) with $\delta^{18,17}O$ plotted above the TF line, except second analysis
502 on F7 that show slightly ^{16}O-rich isotope signatures (Nakashima et al., 2012). Thus, we
503 conclude that silicate fragments in the type A track 22 were disintegrated from single large

minerals/assemblages during the capture, strongly support the origin of type A impactors to be single high strength "rocky" materials (Joswiak et al., 2012).

4.3 Sources of silicate fragments in comet Wild 2

It is known that the ^{16}O-rich ($\Delta^{17}O \sim -23‰$, N=8) Wild 2 fragments, such as Inti (CAI), LIME olivine, and pure forsterite and enstatite, were most likely transported from the refractory inclusion factory at the disk's innermost region to the comet accretion region (>10 AU) by turbulent diffusion during disk expansion (McKeegan et al., 2006; Ciesla, 2007; Nakamura-Messenger et al., 2011; Nakashima et al., 2012; Defouilloy et al., 2017). However, the sources of ^{16}O-poor Wild 2 fragments are less clear. Oxygen and Al-Mg isotope systematics of Wild 2 fragments show close affinities to CR chondrules (Matzel et al., 2010; Nakashima et al., 2012, 2015; Ogliore et al., 2012, 2015; Defouilloy et al., 2017), while Fe-Mn systematics of iron-rich olivines suggest sources of both carbonaceous (CC, mainly CR and CH) and noncarbonaceous (NC, like ordinary chondrite) chondrite regions (Frank et al., 2014; Brownlee and Joswiak, 2017).

As discussed in section 4.2, six (T22/F8, F10, F12, T77/F7, T191/B1/F6, and T220/TP10a/F3; Fo_{60-86}) iron-rich fragments analyzed in this study have positive $\Delta^{17}O$ ($\sim 2‰$) with $\delta^{18,17}O$ plotting on/above the TF line and overlapping with O-E-R chondrules or CH-CB porphyritic chondrules (Figs. 5c, 8). On the Fe vs. Mn diagram (Fig. 4), two falls in the "forbidden triangle" that is only consistent with OC chondrules (Schrader and Davidson, 2022), and four plot close to the trendline of OC chondrules. Similar fragments in the literature are T77/F1, F4, and F5, T22/F7, and "Cecil (TP of T162) (Nakashima et al., 2012; Ogliore et al., 2015). On the $\Delta^{17}O$–Mg# diagram of all Wild 2 fragments analyzed in this study and the literature (Fig. 8), the 11 fragments compose a unique population with

Mg#≤86 and positive $\Delta^{17}O$ of ~+2‰, likely derived from the inner solar system O-E-R chondrules or the outer solar system CH-CB chondrules. The remaining 21 fragments having Mg# ≥79 and negative $\Delta^{17}O$ of ~–2‰, likely derived from a CR chondrule-like environment. The two population overlap at Mg# = 79 to 86 ($\Delta^{17}O$: ~–2‰ to ~+2‰). As exceptions, “Iris" and "Callie" from T74 have Mg#~64 and $\Delta^{17}O$ ~0‰, of which “Iris” is free of live ^{26}Al (“Iris,”>3 Ma after CAI), which are most consistent with CR chondrules (Ogliore et al., 2012; Gainsforth et al., 2015). The proportion of iron-rich fragments with a CR-like source among Wild 2 fragments (2/21, ~10%) is comparable to the abundance of iron-rich chondrules in CR chondrites (~4 vol%) (Schrader et al., 2015). Thus, we conclude that O-E-R- or CH-CB-like materials (11/42, ~26%) contributed to comet Wild 2 as a minor source compared to CR chondrule-like materials (23/42, ~55%) and dominated the iron-rich population with Mg# ≤86.

While minor Wild 2 fragments could have been derived from the inner solar system O-E-R chondrule-forming regions, the astrophysical mechanism that accounts for their outward transportation to the comet accretion region remains uncertain. If the initial formation of chondrules started contemporary with CAIs, as indicated by the bulk ^{207}Pb-^{206}Pb chronology (Bollard et al., 2017), turbulent diffusion could readily transport them outward around the midplane of the protoplanetary disk (Ciesla, 2007). However, in-situ ^{26}Al-^{26}Mg chronology studies indicate ordinary chondrite chondrules formed ~2 Ma after CAIs (Kita et al., 2000; Villeneuve et al., 2009; Kita and Ushikubo, 2012; Pape et al., 2019; Siron et al., 2021, 2022), when a physical barrier (like proto-Jupiter or snowline) had been built up (<1 Ma after CAIs) to limit mixing between inner solar system NC materials and outer solar system CC materials (Kruijer et al., 2017; Lichtenberg et al., 2021). To bypass

the physical barrier, Haugbølle et al. (2019) modeled the inward drift of grains in a circumstellar disk with an embedded planet and found that <300 μm particles could pass through the Jupiter gap, which matches the observed sizes of CAIs in OCs. Based on this result, Schrader et al. (2020) and Schrader and Davidson (2022) argued that small fragments of OC chondrules could permeable the gap and migrate outward through the gap to explain the occurrence of OC-like ($\Delta^{17}O \sim 0‰$) relict olivines and individual chondrules found in carbonaceous chondrites (e.g., Ushikubo et al., 2012; Tenner et al., 2017; Hertwig et al., 2018; Schrader et al., 2020; Williams et al., 2020; Chaumard et al., 2021). It is unclear if this outward-to-inward drift analogy is reasonable because the pressure bump (dust pile-up) was at the outer edge of the gap in an accretion disk (Weber et al., 2018). On the other hand, recent 3D hydrodynamic simulations by Szulágyi et al. (2022) suggest the spiral waves of an embedding planet (>Saturn mass) can drive strong vertical flow and lift the dust onto the circumplanetary region, efficiently bridging over the gap. This meridional circulation of dust and gas around planets has been directly observed around a young star HD 163296 with ALMA (Teague et al., 2019). Thus, the planetary gap is not physically impermeable and could allow both inward and outward dust transportation when the gap is bridged. Furthermore, the Wild 2 fragments that likely came from the inner solar system are micron-sized (<10 μm) that should be well coupled with gas motions, and therefore, can be transported more easily outward and inward without filtering or blocking by any or most barriers.

5. Conclusions

We determined the mineralogy and oxygen isotope ratios of 16 silicate fragments from five type B (T77, T149, T172, T191, and T220) and two type A (T22 and T175)

573 Stardust tracks. Thirteen fragments were exposed by ultramicrotomy. Three subsurface
574 fragments in the resin blocks of T220 were exposed by SIMS Kohler beam (~22 × 22 μm,
575 0.5-1.0 nA) sputtering and then measured for major and minor elements using an FE-EPMA
576 (12 kV, 500 pA) and oxygen isotopes using SIMS (1.5-2.0 μm primary ion beam). The
577 analytical procedure was set up through parallel tests on an SC-Ol grain and a simulant
578 mount of augite standard 7244-Aug, demonstrating its reliability and efficiency of mining
579 subsurface tiny fragments in resin blocks for further mineralogy and oxygen isotope
580 characterizations.

581 Of the 16 silicate fragments, one is a ^{16}O-rich forsterite (Δ^{17}O~–23‰), ten are ^{16}O-
582 poor mono-/polymineralic olivine and low-Ca pyroxene, and three are ^{16}O-poor chondrule-
583 like. The ^{16}O-poor fragments have Mg# ranging from 99 to 60, with six Mg# = 86-60 ones
584 having Δ^{17}O~2‰ and positive $\delta^{18,17}$O that plotted one/above the TF line overlapping with
585 O-E-R chondrules or CH-CB chondrules. Their Fe-Mn systematics are consistent with OC
586 chondrules. Together with five similar fragments from the literature, the 11 fragments
587 compose a unique population characterized by Δ^{17}O~2‰ and Mg#<86, likely genetically
588 related to inner solar system O-E-R chondrules or outer solar system CH-CB chondrules. On
589 the other hand, the remaining nine fragments (Mg# = 95-85) analyzed in this study have
590 Δ^{17}O~–2‰ with $\delta^{18,17}$O plotted on/close to the PCM line. Together with similar fragments
591 in the literature, another population (N=21) characterized by Δ^{17}O~–2‰ and Mg#>79 was
592 identified in contrast to the Mg# <86 population. Minor (N=2, Iris and Calie from T74) iron-
593 rich fragments with Δ^{17}O~0‰ could also belong to this population. Thus, we conclude that
594 O-E-R or CH-CB-like materials (11/42, ~26%) contributed to comet Wild 2 as a minor
595 source compared to CR chondrule-like materials (23/42, ~55%) and dominated the iron-

596 rich population with Mg# ≤86. The outward migration of the inner solar system chondrule-
597 like materials to the comet regions could be possible if there were meridional circulation
598 around giant planets to bridge the gap.

599 For silicate fragments within individual type B tracks, most have consistent $\Delta^{17}O$
600 values (Mg# and/or $\delta^{18,\ 17}O$ values may be different) or display negative $\Delta^{17}O$–Mg#
601 correlation like CR chondrules, while minor show O-E-R or CH-CB chondrule-like
602 signatures. These observations suggest that the impactors of type B tracks are aggregates
603 of unequilibrated fragments derived mostly from similar protoplanetary disk regions with
604 minor exotic, comparable to the cluster IDP U2-20 GCA. Furthermore, four fragments from
605 the type A track 22 have almost identical mineralogy and oxygen isotope ratios, confirming
606 that its impactor is a single chondrule-like fragment.
607
608
609

Acknowledgments

The authors appreciate the assistance with carbon coating by Bil Schneider and with SIMS operation by Michael Spicuzza. We are grateful to Noriyuki Kawasaki, Philipp Heck, and an anonymous reviewer for their very helpful comments and Rhian Jones for editorial handling. This work is supported by the NASA program (NNX16AG80G, N.K.). The WiscSIMS laboratory is supported by NSF (EAR-1658823, -2004618) and UW-Madison. Support for FIB instrumentation was provided by the University of Wisconsin-Madison Office of the Vice-Chancellor for Research and Graduate Education with funding from the Wisconsin Alumni Research Foundation, the College of Engineering, and the NSF Materials Research and Engineering Center (NSF DMR-1121288).

Appendix A. Supplementary material

These supplementary materials are (1) Kohler beam sputtering tests on a SC-Ol grain; (2) Application of the analytical procedure developed for subsurface cometary samples to a simulant mount of 7244-Aug; (3) Low beam current FE-EPMA measurements of olivine and pyroxene reference materials; (4) BSE and SE images of Wild 2 silicate fragments analyzed; and (5) EPMA and oxygen isotope data produced in this study.

Data availability

Data are available through Mendeley Data at https://doi.org/10.17632/j95hc7bm7m.4

References

Berlin J., Jones R. H. and Brearley A. J. (2011) Fe-Mn systematics of type IIA chondrules in unequilibrated CO, CR, and ordinary chondrites. *Meteorit. Planet. Sci* **46**, 513-533.

Bollard J., Connelly J. N., Whitehouse M. J., Pringle E. A., Bonal L., Jørgensen J. K., Nordlund Å., Moynier F. and Bizzarro M. (2017) Early formation of planetary building blocks inferred from Pb isotopic ages of chondrules. *Science Advances* **3**, e1700407.

Bridges J. C., Changela H. G., Nayakshin S., Starkey N. A. and Franchi I. A. (2012) Chondrule fragments from Comet Wild2: Evidence for high temperature processing in the outer Solar System. *Earth Planet. Sci Lett.* **341-344**, 186-194.

Brownlee D., Tsou P., Aléon J., Alexander C. M. O. D., Araki T., Bajt S., Baratta G. A., Bastien R., Bland P., Bleuet P., Borg J., Bradley J. P., Brearley A., Brenker F., Brennan S., Bridges J. C., Browning N. D., Brucato J. R., Bullock E., Burchell M. J., Busemann H., Butterworth A., Chaussidon M., Cheuvront A., Chi M., Cintala M. J., Clark B. C., Clemett S. J., Cody G., Colangeli L., Cooper G., Cordier P., Daghlian C., Dai Z., D'Hendecourt L., Djouadi Z., Dominguez G., Duxbury T., Dworkin J. P., Ebel D. S., Economou T. E., Fakra S., Fairey S. A. J., Fallon S., Ferrini G., Ferroir T., Fleckenstein H., Floss C., Flynn G., Franchi I. A., Fries M., Gainsforth Z., Gallien J.-P., Genge M., Gilles M. K., Gillet P., Gilmour J., Glavin D. P., Gounelle M., Grady M. M., Graham G. A., Grant P. G., Green S. F., Grossemy F., Grossman L., Grossman J. N., Guan Y., Hagiya K., Harvey R., Heck P., Herzog G. F., Hoppe P., Hörz F., Huth J., Hutcheon I. D., Ignatyev K., Ishii H., Ito M., Jacob D., Jacobsen C., Jacobsen S., Jones S., Joswiak D., Jurewicz A., Kearsley A. T., Keller L. P., Khodja H., Kilcoyne A. L. D., Kissel J., Krot A., Langenhorst F., Lanzirotti A., Le L., Leshin L. A., Leitner J., Lemelle L., Leroux H., Liu M.-C., Luening K., Lyon I., MacPherson G., Marcus M. A., Marhas K., Marty B., Matrajt G., McKeegan K., Meibom A., Mennella V., Messenger K., Messenger S., Mikouchi T., Mostefaoui S., Nakamura T., Nakano T., Newville M., Nittler L. R., Ohnishi I., Ohsumi K., Okudaira K., Papanastassiou D. A., Palma R., Palumbo M. E., Pepin R. O., Perkins D., Perronnet M., Pianetta P., Rao W., Rietmeijer F. J. M., Robert F., Rost D., Rotundi A., Ryan R., Sandford S. A., Schwandt C. S., See T. H., Schlutter D., Sheffield-Parker J., Simionovici A., Simon S., Sitnitsky I., Snead C. J., Spencer M. K., Stadermann F. J., Steele A., Stephan T., Stroud R., Susini J., Sutton S. R., Suzuki Y., Taheri M., Taylor S., Teslich N., Tomeoka K., Tomioka N., Toppani A., Trigo-Rodríguez J. M., Troadec D., Tsuchiyama A., Tuzzolino A. J., Tyliszczak T., Uesugi K., Velbel M., Vellenga J., Vicenzi E., Vincze L., Warren J., Weber I., Weisberg M., Westphal A. J., Wirick S., Wooden D., Wopenka B., Wozniakiewicz P., Wright I., Yabuta H., Yano H., Young E. D., Zare R. N., Zega T., Ziegler K., Zimmerman L., Zinner E. and Zolensky M. (2006) Comet 81P/Wild 2 under a microscope. *Science* **314**, 1711-1716.

Brownlee D. E. and Joswiak D. J. (2017) Diversity of the initial rocky planetary building materials at the edge of the solar system. *Meteorit. Planet. Sci* **52**, 471-478.

Burchell M. J., Fairey S. A. J., Wozniakiewicz P., Brownlee D. E., Hörz F., Kearsley A. T., See T. H., Tsou P., Westphal A., Green S. F., Trigo-Rodríguez J. M. and Domingúez G. (2008) Characteristics of cometary dust tracks in Stardust aerogel and laboratory calibrations. *Meteorit. Planet. Sci* **43**, 23-40.

672 Chaumard N., Defouilloy C. and Kita N. T. (2018) Oxygen isotope systematics of chondrules
673 in the Murchison CM2 chondrite and implications for the CO-CM relationship. *Geochim.*
674 *Cosmochim. Acta* **228**, 220-242.
675 Chaumard N., Defouilloy C., Hertwig A. T. and Kita N. T. (2021) Oxygen isotope systematics
676 of chondrules in the Paris CM2 chondrite: Indication for a single large formation
677 region across snow line. *Geochim. Cosmochim. Acta* **299**, 199-218.
678 Ciesla F. J. (2007) Outward transport of high-temperature materials around the midplane
679 of the solar nebula. *Science* **318**, 613-615.
680 Connolly J. H. C. and Huss G. R. (2010) Compositional evolution of the protoplanetary disk:
681 Oxygen isotopes of type-II chondrules from CR2 chondrites. *Geochim. Cosmochim. Acta*
682 **74**, 2473-2483.
683 Defouilloy C., Nakashima D., Joswiak D. J., Brownlee D. E., Tenner T. J. and Kita N. T. (2017)
684 Origin of crystalline silicates from Comet 81P/Wild 2: Combined study on their oxygen
685 isotopes and mineral chemistry. *Earth Planet. Sci Lett.* **465**, 145-154.
686 Demers H., Poirier-Demers N., Couture A. R., Joly D., Guilmain M., de Jonge N., and Drouin D.
687 (2011) Three-dimensional electron microscopy simulation with the CASINO Monte
688 Carlo software. *Scanning* **33**: 135-146.
689 Donovan J. J., Singer J. W., Armstrong, J. T. (2016) A new EPMA method for fast trace
690 element analysis in simple matrices. *Am. Minearl.* **101**: 1839-1853.
691 Donovan J. J., Moy A., von der Handt A., Gainsforth Z., Maner J. L., Nachlas W. and Fournelle J.
692 (2023) A New Method for Dead Time Calibration and a New Expression for Correction
693 of WDS Intensities for Microanalysis. *Microscopy and Microanalysis* **29**, 1096-1110.
694 Floss C., Stadermann F. J., Kearsley A. T., Burchell M. J. and Ong W. (2013) The abundance of
695 presolar grains in comet 81P/Wild 2. *Astrophys. J.* **763**, 140.
696 Frank D. R., Zolensky M. E. and Le L. (2014) Olivine in terminal particles of Stardust aerogel
697 tracks and analogous grains in chondrite matrix. *Geochim. Cosmochim. Acta* **142**, 240-
698 259.
699 Fukuda K., Beard B. L., Dunlap D. R., Spicuzza M. J., Fournelle J. H., Wadhwa M. and Kita N. T.
700 (2020) Magnesium isotope analysis of olivine and pyroxene by SIMS: Evaluation of
701 matrix effects. *Chem. Geol* **540**, 119482.
702 Fukuda K., Brownlee D. E., Joswiak D. J., Tenner T. J., Kimura M. and Kita N. T. (2021)
703 Correlated isotopic and chemical evidence for condensation origins of olivine in comet
704 81P/Wild 2 and in AOAs from CV and CO chondrites. *Geochim. Cosmochim. Acta* **293**,
705 544-574.
706 Fukuda, K., Tenner T. J., Kimura M., Tomioka N., Siron G., Ushikubo T., Chaumard N.,
707 Hertwig A. T., and Kita N. T. (2022) A temporal shift of chondrule generation from the
708 inner to outer Solar System inferred from oxygen isotopes and Al-Mg chronology of
709 chondrules from primitive CM and CO chondrites. *Geochim. Cosmochim. Acta* **322**, 194-
710 226.
711 Gainsforth Z., Butterworth A. L., Stodolna J., Westphal A. J., Huss G. R., Nagashima K., Ogliore
712 R., Brownlee D. E., Joswiak D., Tyliszczak T. and Simionovici A. S. (2015) Constraints on
713 the formation environment of two chondrule-like igneous particles from comet
714 81P/Wild 2. *Meteorit. Planet. Sci* **50**, 976-1004.

715 Gainsforth Z., Westphal A. J., Butterworth A. L., Jilly-Rehak C. E., Brownlee D. E., Joswiak D. J.,
716 Ogliore R. C., Zolensky M. E., Bechtel H. A., Ebel D. S., Huss G. R., Sandford S. A. and
717 White A. J. (2019) Fine-grained material associated with a large sulfide returned from
718 Comet 81P/Wild 2. *Meteorit. Planet. Sci* **54**, 1069-1091.

719 Gauvin R., Lifshin E., Demers H., Horny P. and Campbell H. (2006) Win X-ray: A new Monte
720 Carlo program that computes X-ray spectra obtained with a scanning electron
721 microscope. *Microscopy and Microanalysis* **12**, 49-64.

722 Haugbølle T., Weber P., Wielandt D. P., Benítez-Llambay P., Bizzarro M., Gressel O. and
723 Pessah M. E. (2019) Probing the Protosolar Disk Using Dust Filtering at Gaps in the
724 Early Solar System. *Astrophys. J.* **158**, 55.

725 Heck P. R., Ushikubo T., Schmitz B., Kita N. T., Spicuzza M. J. and Valley J. W. (2010) A single
726 asteroidal source for extraterrestrial Ordovician chromite grains from Sweden and
727 China: High-precision oxygen three-isotope SIMS analysis. *Geochim. Cosmochim. Acta*
728 **74**, 497-509.

729 Hertwig A. T., Defouilloy C. and Kita N. T. (2018) Formation of chondrules in a moderately
730 high dust enriched disk: evidence from oxygen isotopes of chondrules from the Kaba
731 CV3 chondrite. *Geochim. Cosmochim. Acta* **224**, 116-131.

732 Hertwig A. T., Kimura M., Defouilloy C. and Kita N. T. (2019) Oxygen isotope systematics of
733 chondrule olivine, pyroxene, and plagioclase in one of the most pristine CV3Red
734 chondrites (Northwest Africa 8613). *Meteorit. Planet. Sci* **54**, 2666-2685.

735 Hörz F., Bastien R., Borg J., Bradley J. P., Bridges J. C., Brownlee D. E., Burchell M. J., Chi M.,
736 Cintala M. J., Dai Z. R., Djouadi Z., Dominguez G., Economou T. E., Fairey S. A. J., Floss C.,
737 Franchi I. A., Graham G. A., Green S. F., Heck P., Hoppe P., Huth J., Ishii H., Kearsley A. T.,
738 Kissel J., Leitner J., Leroux H., Marhas K., Messenger K., Schwandt C. S., See T. H., Snead
739 C., Stadermann F. J., Stephan T., Stroud R., Teslich N., Trigo-Rodríguez J. M., Tuzzolino
740 A. J., Troadec D., Tsou P., Warren J., Westphal A., Wozniakiewicz P., Wright I. and
741 Zinner E. (2006) Impact features on stardust: Implications for comet 81P/Wild 2 dust.
742 *Science* **314**, 1716-1719.

743 Ishii H. A., Bradley J. P., Dai Z. R., Chi M., Kearsley A. T., Burchell M. J., Browning N. D. and
744 Molster F. (2008) Comparison of comet 81P/Wild 2 dust with interplanetary dust
745 from comets. *Science* **319**, 447-450.

746 Joswiak D. J., Brownlee D. E., Matrajt G., Westphal A. J. and Snead C. J. (2009) Kosmochloric
747 Ca-rich pyroxenes and FeO-rich olivines (Kool grains) and associated phases in
748 Stardust tracks and chondritic porous interplanetary dust particles: Possible
749 precursors to FeO-rich type II chondrules in ordinary chondrites. *Meteorit. Planet. Sci*
750 **44**, 1561-1588.

751 Joswiak D. J., Brownlee D. E., Matrajt G., Westphal A. J., Snead C. J. and Gainsforth Z. (2012)
752 Comprehensive examination of large mineral and rock fragments in Stardust tracks:
753 Mineralogy, analogous extraterrestrial materials, and source regions. *Meteorit. Planet.*
754 *Sci* **47**, 471-524.

755 Joswiak D. J., Nakashima D., Brownlee D. E., Matrajt G., Ushikubo T., Kita N. T., Messenger S.
756 and Ito M. (2014) Terminal particle from Stardust track 130: Probable Al-rich
757 chondrule fragment from comet Wild 2. *Geochim. Cosmochim. Acta* **144**, 277-298.

758 Joswiak D. J., Brownlee D. E., Nguyen A. N. and Messenger S. (2017) Refractory materials in
759 comet samples. *Meteorit. Planet. Sci* **52**, 1612-1648.
760 Kearsley A. T., Burchell M. J., Hörz F., Cole M. J. and Schwandt C. S. (2006) Laboratory
761 simulation of impacts on aluminum foils of the Stardust spacecraft: Calibration of dust
762 particle size from comet Wild-2. *Meteorit. Planet. Sci* **41**, 167-180.
763 Kita N. T., Nagahara H., Togashi S. and Morishita Y. (2000) A short duration of chondrule
764 formation in the solar nebula: evidence from ^{26}Al in Semarkona ferromagnesian
765 chondrules. *Geochim. Cosmochim. Acta* **64**, 3913-3922.
766 Kita N. T., Ushikubo T., Fu B. and Valley J. W. (2009) High precision SIMS oxygen isotope
767 analysis and the effect of sample topography. *Chem. Geol* **264**, 43-57.
768 Kita N. T., Nagahara H., Tachibana S., Tomomura S., Spicuzza M. J., Fournelle J. H. and Valley
769 J. W. (2010) High precision SIMS oxygen three isotope study of chondrules in LL3
770 chondrites: Role of ambient gas during chondrule formation. *Geochim. Cosmochim.*
771 *Acta* **74**, 6610-6635.
772 Kita N. T. and Ushikubo T. (2012) Evolution of protoplanetary disk inferred from ^{26}Al
773 chronology of individual chondrules. *Meteorit. Planet. Sci* **47**, 1108-1119.
774 Kita N. T., Sobol P. E., Kern J. R., Lord N. E. and Valley J. W. (2015) UV-light microscope:
775 improvements in optical imaging for a secondary ion mass spectrometer. *J. Anal. At.*
776 *Spectrom.* **30**, 1207-1213.
777 Krot A. N., Nagashima K., Yoshitake M. and Yurimoto H. (2010) Oxygen isotopic
778 compositions of chondrules from the metal-rich chondrites Isheyevo (CH/CBb), MAC
779 02675 (CBb) and QUE 94627 (CBb). *Geochim. Cosmochim. Acta* **74**, 2190-2211.
780 Kruijer T. S., Burkhardt C., Budde G. and Kleine T. (2017) Age of Jupiter inferred from the
781 distinct genetics and formation times of meteorites. *Proc. Natl. Acad. Sci.* **114**, 6712-
782 6716.
783 Lichtenberg T., Drążkowska J., Schönbächler M., Golabek G. J. and Hands T. O. (2021)
784 Bifurcation of planetary building blocks during Solar System formation. *Science* **371**,
785 365-370.
786 Linzmeier B., Kitajima K., Denny A. and Cammack J. (2018) Making maps on a micrometer
787 scale. *Eos* **99**.
788 Marrocchi Y., Villeneuve J., Jacquet E., Piralla M. and Chaussidon M. (2019) Rapid
789 condensation of the first Solar System solids. *Proc. Natl. Acad. Sci.*, 201912479.
790 Matrajt G. and Brownlee D. E. (2006) Acrylic embedding of Stardust particles encased in
791 aerogel. *Meteorit. Planet. Sci* **41**, 1715-1720.
792 Matzel J. E. P., Ishii H. A., Joswiak D., Hutcheon I. D., Bradley J. P., Brownlee D., Weber P. K.,
793 Teslich N., Matrajt G., McKeegan K. D. and MacPherson G. J. (2010) Constraints on the
794 Formation Age of Cometary Material from the NASA Stardust Mission. *Science* **328**,
795 483-486.
796 McKeegan K. D., Aléon J., Bradley J., Brownlee D., Busemann H., Butterworth A., Chaussidon
797 M., Fallon S., Floss C. and Gilmour J. (2006) Isotopic compositions of cometary matter
798 returned by Stardust. *Science* **314**, 1724-1728.

Messenger S. (2000) Identification of molecular-cloud material in interplanetary dust particles. *Nature* **404**, 968-971.

Miller K. E., Lauretta D. S., Connolly H. C., Berger E. L., Nagashima K. and Domanik K. (2017) Formation of unequilibrated R chondrite chondrules and opaque phases. *Geochim. Cosmochim. Acta* **209**, 24-50.

Nagashima K., Krot A. N. and Huss G. R. (2014) ^{26}Al in chondrules from CR2 chondrites. *Geochem. J.* **48**, 561-570.

Nakamura-Messenger K., Keller L. P., Clemett S. J., Messenger S. and Ito M. (2011) Nanometer-scale anatomy of entire Stardust tracks. *Meteorit. Planet. Sci* **46**, 1033-1051.

Nakamura T., Noguchi T., Tsuchiyama A., Ushikubo T., Kita N. T., Valley J. W., Zolensky M. E., Kakazu Y., Sakamoto K., Mashio E., Uesugi K. and Nakano T. (2008) Chondrulelike objects in short-period comet 81P/Wild 2. *Science* **321**, 1664-1667.

Nakashima D., Ushikubo T., Joswiak D. J., Brownlee D. E., Matrajt G., Weisberg M. K., Zolensky M. E. and Kita N. T. (2012) Oxygen isotopes in crystalline silicates of comet Wild 2: A comparison of oxygen isotope systematics between Wild 2 particles and chondritic materials. *Earth Planet. Sci Lett.* **357-358**, 355-365.

Nakashima D., Ushikubo T., Kita N. T., Weisberg M. K., Zolensky M. E. and Ebel D. S. (2015) Late formation of a comet Wild 2 crystalline silicate particle, Pyxie, inferred from Al–Mg chronology of plagioclase. *Earth Planet. Sci Lett.* **410**, 54-61.

Ogliore R. C., Huss G. R., Nagashima K., Butterworth A. L., Gainsforth Z., Stodolna J., Westphal A. J., Joswiak D. and Tyliszczak T. (2012) Incorporation of a late-forming chondrule into comet Wild 2. *Astrophys. J.* **745**, L19.

Ogliore R. C., Nagashima K., Huss G. R., Westphal A. J., Gainsforth Z. and Butterworth A. L. (2015) Oxygen isotopic composition of coarse- and fine-grained material from comet 81P/Wild 2. *Geochim. Cosmochim. Acta* **166**, 74-91.

Ogliore R. C., Palma R. L., Stodolna J., Nagashima K., Pepin R. O., Schlutter D. J., Gainsforth Z., Westphal A. J. and Huss G. R. (2019) Q-Gases in a Late-Forming Refractory Interplanetary Dust Particle: A Link to Comet Wild 2. *Geochim. Cosmochim. Acta* **271**, 116-131.

Pape J., Mezger K., Bouvier A. S. and Baumgartner L. P. (2019) Time and duration of chondrule formation: Constraints from ^{26}Al-^{26}Mg ages of individual chondrules. *Geochim. Cosmochim. Acta* **244**, 416-436.

Schrader D. L., Connolly H. C., Lauretta D. S., Nagashima K., Huss G. R., Davidson J. and Domanik K. J. (2013) The formation and alteration of the Renazzo-like carbonaceous chondrites II: Linking O-isotope composition and oxidation state of chondrule olivine. *Geochim. Cosmochim. Acta* **101**, 302-327.

Schrader D. L., Nagashima K., Krot A. N., Ogliore R. C. and Hellebrand E. (2014) Variations in the O-isotope composition of gas during the formation of chondrules from the CR chondrites. *Geochim. Cosmochim. Acta* **132**, 50-74.

Schrader D. L., Connolly Jr. H. C., Lauretta D. S., Zega T. J., Davidson J. and Domanik K. J. (2015) The formation and alteration of the Renazzo-like carbonaceous chondrites III:

Toward understanding the genesis of ferromagnesian chondrules. *Meteorit. Planet. Sci* **50**, 15-50.

Schrader D. L., Nagashima K., Krot A. N., Ogliore R. C., Yin Q.-Z., Amelin Y., Stirling C. H. and Kaltenbach A. (2017) Distribution of ^{26}Al in the CR chondrite chondrule-forming region of the protoplanetary disk. *Geochim. Cosmochim. Acta* **201**, 275-302.

Schrader D. L., Nagashima K., Davidson J., McCoy T. J., Ogliore R. C. and Fu R. R. (2020) Outward migration of chondrule fragments in the Early Solar System: O-isotopic evidence for rocky material crossing the Jupiter Gap? *Geochim. Cosmochim. Acta* **282**, 133-155.

Schrader D. L. and Davidson J. (2022) Prolonged early migration of dust from the inner Solar System to the comet-forming region. *Earth Planet. Sci Lett.* **589**, 117552.

Simon S. B., Joswiak D. J., Ishii H. A., Bradley J. P., Chi M., Grossman L., Aleon J., Brownlee D. E., Fallon S., Hutcheon I. D., Matrajt G. and McKeegan K. D. (2008) A refractory inclusion returned by Stardust from comet 81P/Wild 2. *Meteorit. Planet. Sci* **43**, 1861-1877.

Siron G., Fukuda K., Kimura M. and Kita N. T. (2021) New constraints from ^{26}Al-^{26}Mg chronology of anorthite bearing chondrules in unequilibrated ordinary chondrites. *Geochim. Cosmochim. Acta* **293**, 103-126.

Siron G., Fukuda K., Kimura M. and Kita N. T. (2022) High precision ^{26}Al-^{26}Mg chronology of chondrules in unequilibrated ordinary chondrites: Evidence for restricted formation ages. *Geochim. Cosmochim. Acta* **324**, 312-345.

Stodolna J., Gainsforth Z., Butterworth A. L. and Westphal A. J. (2014) Characterization of preserved primitive fine-grained material from the Jupiter family comet 81P/Wild 2 – A new link between comets and CP-IDPs. *Earth Planet. Sci Lett.* **388**, 367-373.

Szulágyi J., Binkert F. and Surville C. (2022) Meridional circulation of dust and gas in the circumstellar disk: Delivery of solids onto the circumplanetary region. *Astrophys. J.* **924**, 1.

Teague R., Bae J. and Bergin E. A. (2019) Meridional flows in the disk around a young star. *Nature* **574**, 378-381.

Tenner T. J., Ushikubo T., Kurahashi E., Kita N. T. and Nagahara H. (2013) Oxygen isotope systematics of chondrule phenocrysts from the CO3.0 chondrite Yamato 81020: Evidence for two distinct oxygen isotope reservoirs. *Geochim. Cosmochim. Acta* **102**, 226-245.

Tenner T. J., Nakashima D., Ushikubo T., Kita N. T. and Weisberg M. K. (2015) Oxygen isotope ratios of FeO-poor chondrules in CR3 chondrites: Influence of dust enrichment and H_2O during chondrule formation. *Geochim. Cosmochim. Acta* **148**, 228-250.

Tenner T. J., Kimura M. and Kita N. T. (2017) Oxygen isotope characteristics of chondrules from the Yamato-82094 ungrouped carbonaceous chondrite: Further evidence for common O-isotope environments sampled among carbonaceous chondrites. *Meteorit. Planet. Sci* **52**, 268-294.

Tenner T. J., Nakashima D., Ushikubo T., Tomioka N., Kimura M., Weisberg M. K. and Kita N. T. (2019) Extended chondrule formation intervals in distinct physicochemical

environments: Evidence from Al-Mg isotope systematics of CR chondrite chondrules with unaltered plagioclase. *Geochim. Cosmochim. Acta* **260**, 133-160.

Thomas K. L., Blanford G. E., Clemett S. J., Flynn G. J., Keller L. P., Klöck W., Maechling C. R., Mc Kay D. S., Messenger S., Nier A. O., Schlutter D. J., Sutton S. R., Warren J. L. and Zare R. N. (1995) An asteroidal breccia: The anatomy of a cluster IDP. *Geochim. Cosmochim. Acta* **59**, 2797-2815.

Tomeoka K., Tomioka N. and Ohnishi I. (2008) Silicate minerals and Si-O glass in comet Wild 2 samples: Transmission electron microscopy. *Meteorit. Planet. Sci* **43**, 273-284.

Ushikubo T., Kimura M., Kita N. T. and Valley J. W. (2012) Primordial oxygen isotope reservoirs of the solar nebula recorded in chondrules in Acfer 094 carbonaceous chondrite. *Geochim. Cosmochim. Acta* **90**, 242-264.

Ushikubo T., Tenner T. J., Hiyagon H. and Kita N. T. (2017) A long duration of the ^{16}O-rich reservoir in the solar nebula, as recorded in fine-grained refractory inclusions from the least metamorphosed carbonaceous chondrites. *Geochim. Cosmochim. Acta* **201**, 103-122.

Ushikubo T. and Kimura M. (2021) Oxygen-isotope systematics of chondrules and olivine fragments from Tagish Lake C2 chondrite: Implications of chondrule-forming regions in protoplanetary disk. *Geochim. Cosmochim. Acta* **293**, 328-343.

Utt K. L., Ogliore R. C., Liu N., Krot A. N., Bradley J. P., Brownlee D. E. and Joswiak D. J. (2023) Diverse oxygen isotopic compositions among cometary vapor-phase condensates. *Geochim. Cosmochim. Acta* **343**, 250-263.

Villeneuve J., Chaussidon M. and Libourel G. (2009) Homogeneous distribution of ^{26}Al in the solar system from the Mg isotopic composition of chondrules. *Science* **325**, 985-988.

Weber P., Benítez-Llambay P., Gressel O., Krapp L. and Pessah M. E. (2018) Characterizing the variable dust permeability of planet-induced gaps. *Astrophys. J.* **854**, 153.

Weisberg M. K., Ebel D. S., Connolly H. C., Kita N. T. and Ushikubo T. (2011) Petrology and oxygen isotope compositions of chondrules in E3 chondrites. *Geochim. Cosmochim. Acta* **75**, 6556-6569.

Weisberg M. K., Kita N. T., Fukuda K., Siron G. and Ebel D. S. (2021) Micro-distribution of oxygen isotopes in unequilibrated enstatite chondrites. *Geochim. Cosmochim. Acta* **300**, 279-295.

Westphal A. J., Snead C., Butterworth A., Graham G. A., Bradley J. P., Bajt S., Grant P. G., Bench G., Brennan S. and Pianetta P. (2004) Aerogel keystones: Extraction of complete hypervelocity impact events from aerogel collectors. *Meteorit. Planet. Sci* **39**, 1375-1386.

Westphal A. J., Fakra S. C., Gainsforth Z., Marcus M. A., Ogliore R. C. and Butterworth A. L. (2009) Mixing fraction of inner solar system material in Comet 81P/Wild2. *Astrophys. J.* **694**, 18.

Williams C. D., Sanborn M. E., Defouilloy C., Yin Q.-Z., Kita N. T., Ebel D. S., Yamakawa A. and Yamashita K. (2020) Chondrules reveal large-scale outward transport of inner solar system materials in the protoplanetary disk. *Proc. Natl. Acad. Sci.* **117**, 23426-23435.

Zhang M., Defouilloy C., Joswiak D. J., Brownlee D. E., Nakashima D., Siron G., Kitajima K. and Kita N. T. (2021) Oxygen isotope systematics of crystalline silicates in a giant cluster

IDP: A genetic link to Wild 2 particles and primitive chondrite chondrules. *Earth Planet. Sci Lett.* **564**, 116928.

Zhang M., Fukuda K., Spicuzza M. J., Siron G., Heimann A., Hammerstrom A. J., Kita N. T., Ushikubo T. and Valley J. W. (2022) SIMS matrix effects in oxygen isotope analysis of olivine and pyroxene: Application to Acfer 094 chondrite chondrules and reconsideration of the primitive chondrule minerals (PCM) line. *Chem. Geol* **608**, 121016.

Zolensky M. E., Zega T. J., Yano H., Wirick S., Westphal A. J., Weisberg M. K., Weber I., Warren J. L., Velbel M. A., Tsuchiyama A., Tsou P., Toppani A., Tomioka N., Tomeoka K., Teslich N., Taheri M., Susini J., Stroud R., Stephan T., Stadermann F. J., Snead C. J., Simon S. B., Simionovici A., See T. H., Robert F., Rietmeijer F. J. M., Rao W., Perronnet M. C., Papanastassiou D. A., Okudaira K., Ohsumi K., Ohnishi I., Nakamura-Messenger K., Nakamura T., Mostefaoui S., Mikouchi T., Meibom A., Matrajt G., Marcus M. A., Leroux H., Lemelle L., Le L., Lanzirotti A., Langenhorst F., Krot A. N., Keller L. P., Kearsley A. T., Joswiak D., Jacob D., Ishii H., Harvey R., Hagiya K., Grossman L., Grossman J. N., Graham G. A., Gounelle M., Gillet P., Genge M. J., Flynn G., Ferroir T., Fallon S., Ebel D. S., Dai Z. R., Cordier P., Clark B., Chi M., Butterworth A. L., Brownlee D. E., Bridges J. C., Brennan S., Brearley A., Bradley J. P., Bleuet P., Bland P. A. and Bastien R. (2006) Mineralogy and petrology of comet 81P/Wild 2 nucleus samples. *Science* **314**, 1735-1739.

Figure Captions

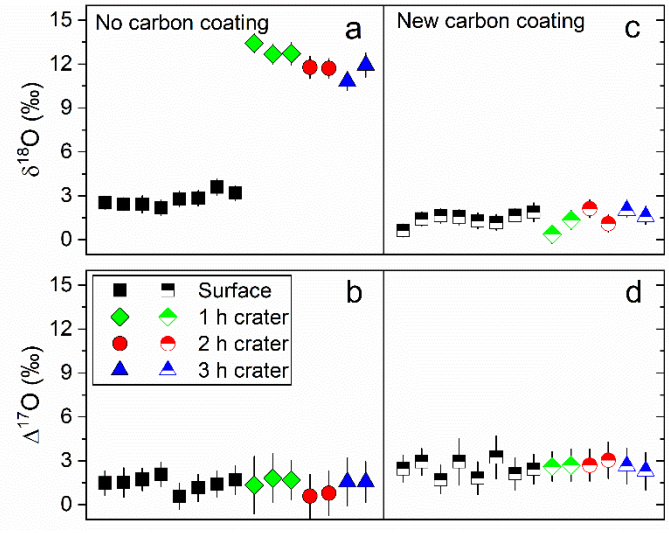

Fig. 1. Oxygen isotope analyses on the flat bottom of SIMS Kohler beam craters with/without a new carbon coating and on the polished surface of an SC-Ol grain. The craters were made by 1-, 2-, and 3-hour Kohler beam (~1 nA, ~22 × 22 μm^2) sputtering, which have depths of ~2.3 μm, ~4.6 μm, and ~6 μm, respectively. Error bars for $\delta^{18}O$ and $\Delta^{17}O$ are internal errors (2SE) of individual analysis, typically 0.5 ‰ and 1.0 ‰, respectively. The analytical condition, ~3 μm Gaussian beam with an intensity of ~20 pA, was similar to that described in Ushikubo et al. (2012). No oxygen isotope fractionation difference between the crater bottom and the polished surface after applying a new carbon coating, regardless of the crater depth (≤ 6 μm deep for a ~22 × 22 μm Kohler beam to avoid the shadow effect of the beam crater due to the ~21° inclination angle of the primary ion column).

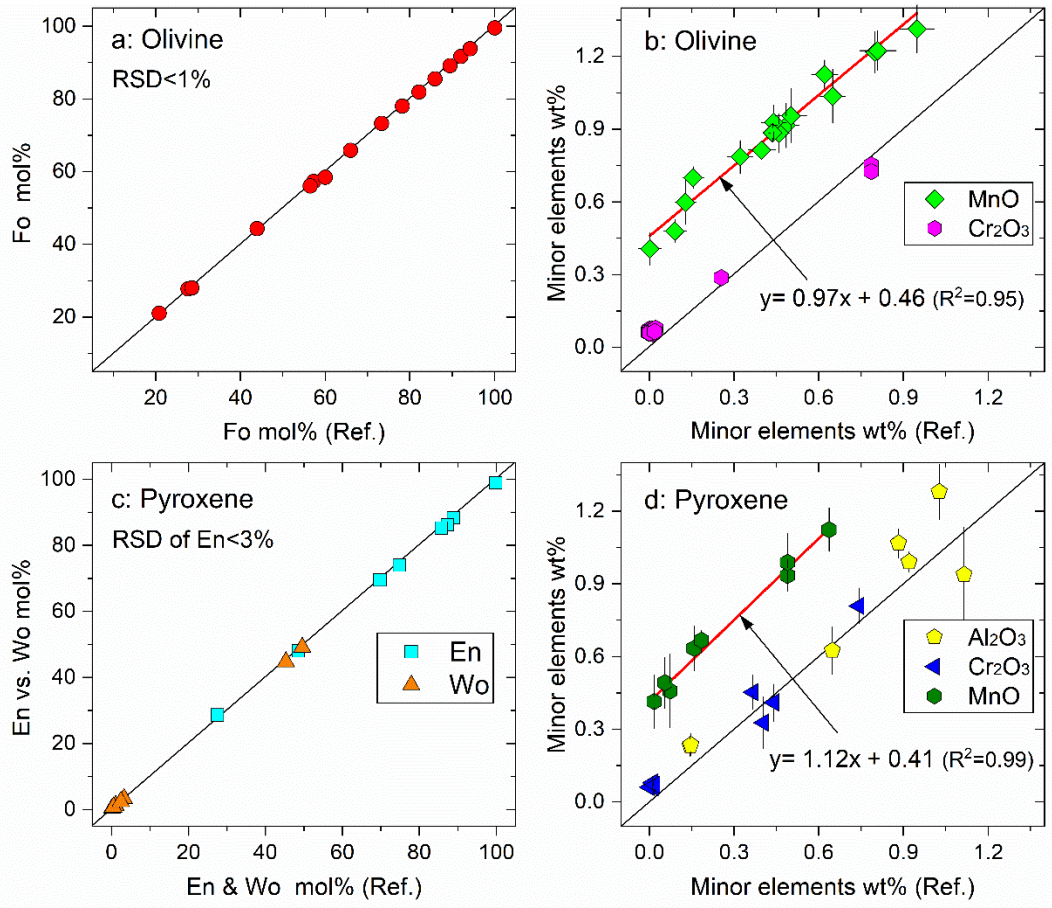

962

963 Fig. 2. Evaluation of analytical precision of an FE-EPMA under 12 kV, 500 pA condition
964 using a series of olivine and pyroxene standards. The reference values for these olivine and
965 pyroxene standards were reported by Fukuda et al. (2020) and Zhang et al. (2022). RSD =
966 relative standard deviation. Regression lines were drawn for MnO contents in olivine and
967 pyroxene, which are systematically higher than their reference values.

968

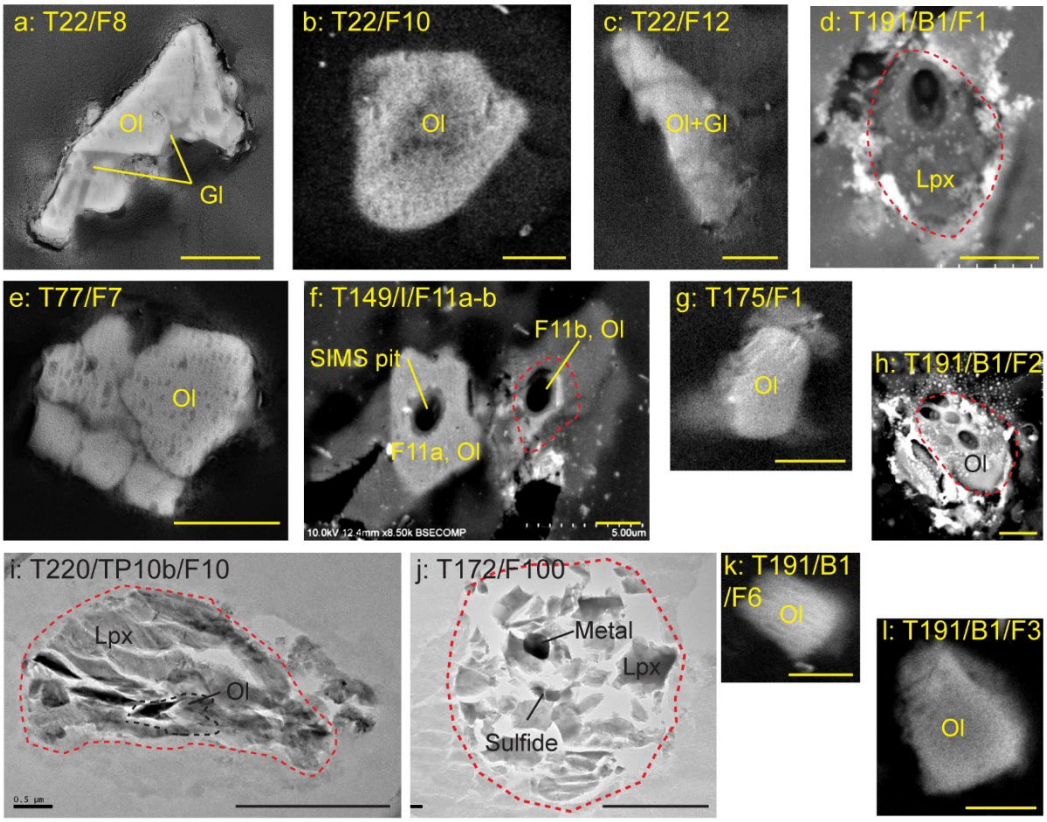

969

970 Fig. 3. Backscattered (BSE, a-h, k-l) and TEM bright field (i-j) images of Wild 2 fragments
971 exposed by ultramicrotomy. The scale bar is 2 μm. Oval craters in panels d, f, and h are
972 SIMS analysis pits. Abbreviation: Ol = olivine; Lpx = low-Ca pyroxene; Gl = glassy
973 mesostasis.

974

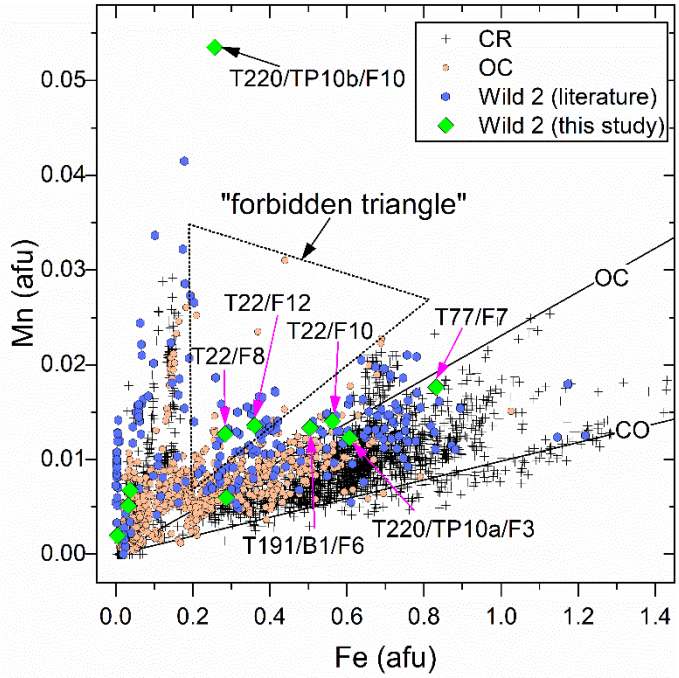

975

976 Fig. 4. Mn versus Fe (afu = atomic formula units based on four oxygen atoms) for Wild 2
977 olivines in this study. The OC and CO chondrules trend lines are adopted from Berlin et al.
978 (2011). Data for CR chondrules (Schrader et al., 2015), OC chondrules (Schrader and
979 Davidson, 2022), other Wild 2 fragments, and anhydrous IDPs (Brownlee and Joswiak,
980 2017; Zhang et al., 2021) are plotted for comparison. The "forbidden triangle" is adopted
981 from Brownlee and Joswiak (2017) and Schrader and Davidson (2022). The magenta
982 arrows indicate those particles with positive oxygen isotope ratios that plot on/above the
983 terrestrial fractionation (TF) line (as shown in Fig. 5c). The dark arrow indicates the olivine
984 inclusion in T220/TP10B/F10, which has distinctly Mn-rich compared to other Wild 2
985 olivines except for the fayalite in the terminal particles (named "Ada") of track 26 (Joswiak
986 et al., 2012).

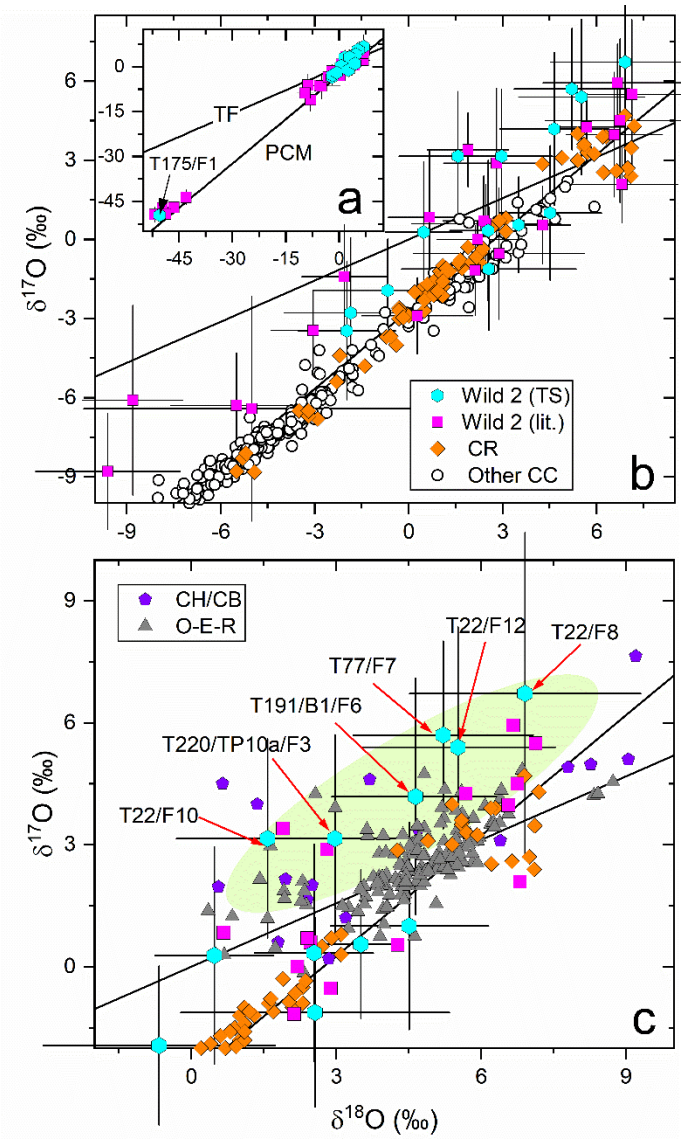

Fig. 5. Oxygen isotope ratios of Wild 2 silicate fragments (TS = this study; Lit. = literature) compared with primitive chondrite chondrules. Data source: Wild 2 (Nakamura et al., 2008; Nakashima et al., 2012; Ogliore et al., 2012, 2015; Joswiak et al., 2014; Gainsforth et al., 2015; Defouilloy et al., 2017), CV (Hertwig et al., 2018, 2019), CO (Tenner et al., 2013; Fukuda et al., 2022), CM (Chaumard et al., 2018, 2021), CA (Tenner et al., 2017), Acfer 094 (Ushikubo et al., 2012), Tagish Lake (Ushikubo and Kimura, 2021), ordinary (O) (Kita et al., 2010; Siron et al., 2021, 2022), enstatite (E) (Weisberg et al., 2011, 2021), Rumuruti (R)

995 (Miller et al., 2017), CH-CB (Krot et al., 2010), and CR chondrites (Connolly and Huss, 2010;
996 Schrader et al., 2013, 2014; Tenner et al., 2015). The red arrows indicate the six Wild 2
997 fragments that show positive oxygen isotope ratios overlapping with some chondrules in
998 O-E-R and CH-CB chondrites (the green region in c). TF = terrestrial fractionation line. PCM
999 = primitive chondrule minerals (PCM) line (Ushikubo et al., 2012).

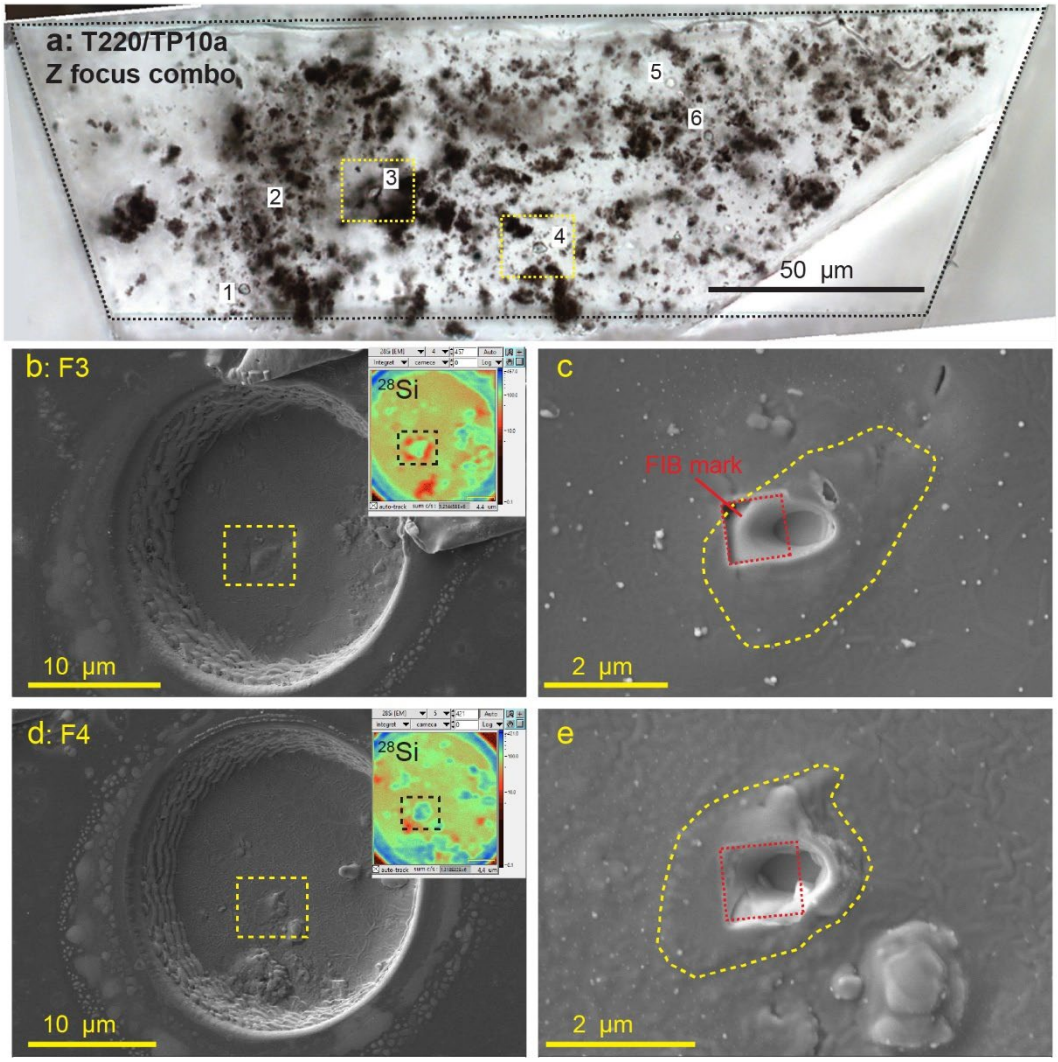

Fig. 6. Analytical procedure demo for subsurface Wild 2 fragments in an acrylic block of T220. (a) Z focus-combined transmitted light image of the resin block before mounting into indium. Fragments 3, 4, and 5 are estimated to be >2 μm in size and 2-8 μm deep under an optical microscope. (b, d) SE images of Kohler beam pits where F3 (exposed size is 3 × 1.5 μm, depth is 7.8 μm) and F4 (exposed size is 2.5 × 1.8 μm, depth is 4.5 μm) are located. Insets show the Ion images of $^{28}Si^-$, from which the exposed sizes of F3 and F4 were estimated. (c, e) SE images of SIMS pit on F3 and F4. The pits are ~1.5 × 1 μm in size with a flat bottom. The red rectangles show the locations of the FIB marks, which were used as

1009 references to locate the target fragments during SIMS oxygen isotope analysis. EPMA
1010 analyses on these fragments were done before FIB marking.

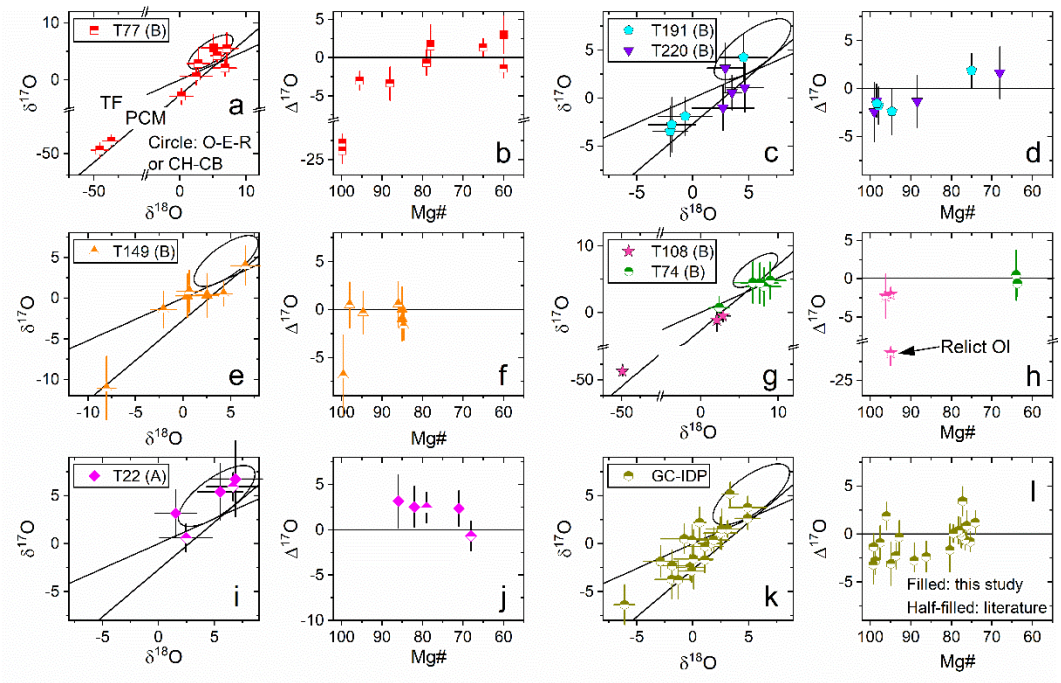

Fig. 7. Oxygen isotope systematics of Wild 2 silicate fragments in individual tracks, compared to silicate fragments from the giant cluster (GC)-IDP U2-20-GCA (Brownlee and Joswiak, 2017; Zhang et al., 2021). Wild 2 fragments analyzed in this study are shown in filled symbols, while those from the literature are shown in half-filled symbols. The oxygen isotope region for those O-E-R and CH-CB chondrules above the TF line is outlined by a black circle. The track type (A/B) is shown in the bracket after the track number. Data source: this study, Nakamura et al. (2008), Nakashima et al. (2012), Ogliore et al. (2012, 2015), Gainsforth et al. (2015), and Defouilloy et al. (2017). The relict olivine ($\Delta^{17}O \sim -23‰$) in T108 "Gozen-sama" was indicated. Multiple analyses on "Iris" (N=3) from track 74 and F7 (N=2) of track 22 were plotted because of their resolvable oxygen isotope differences, while other fragments were denoted as single data spots. TF = terrestrial fractionation line. PCM = primitive chondrule minerals (PCM) line (Ushikubo et al., 2012).

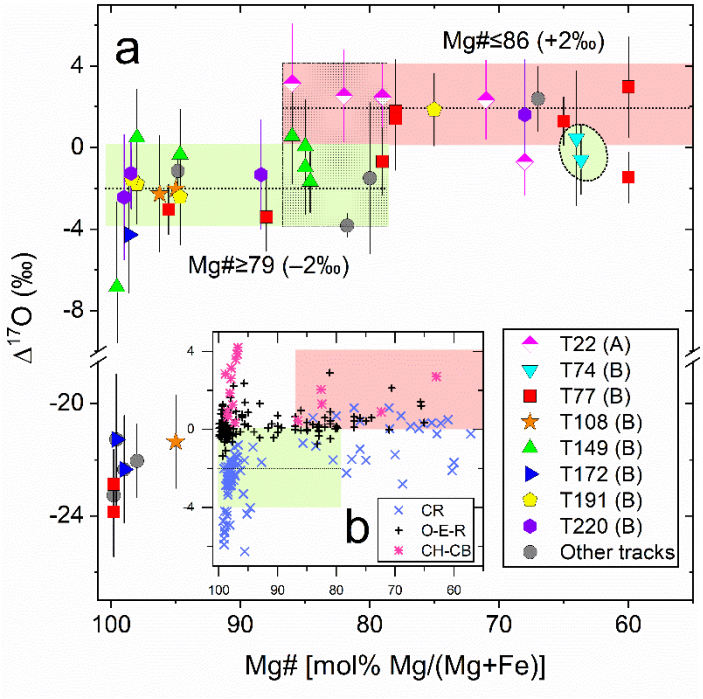

1024

1025 Fig. 8. Mg#–$\Delta^{17}O$ relationship for Wild 2 silicate fragments analyzed in this study and the
1026 literature (Nakamura et al., 2008; Nakashima et al., 2012; Ogliore et al., 2012, 2015;
1027 Joswiak et al., 2014; Gainsforth et al., 2015; Defouilloy et al., 2017). Aerogel tracks with
1028 multiple fragments analyzed are shown in different symbols, and tracks with only one
1029 fragment studied are grouped as "other tracks." Two groups of Wild 2 fragments can be
1030 identified; one (pink) has Mg# ≤86 and $\Delta^{17}O$~+2‰ that could be related to inner solar
1031 system O-E-R chondrules or out solar system CH-CB chondrules, including the six
1032 fragments marked in Fig. 5c of this study, and five fragments (T22/F7, T77/F1, F4, and F5,
1033 T162 "Cecil") in the literature; the other (yellow-green) has Mg#≥79 and $\Delta^{17}O$~–2‰ that
1034 are most consistent with CR chondrite chondrules. Noteworthy, the two iron-rich
1035 fragments ("Iris" and "Callie" from T74, emerald green) with ~0‰ $\Delta^{17}O$ and no resolvable
1036 ^{26}Mg excess (Iris, Ogliore et al., 2012) are also CR chondrule-like. In panel b, O-E-R, CR, and
1037 CH-CB chondrules are plotted for comparison (Connolly and Huss, 2010; Krot et al., 2010;

Weisberg et al., 2011, 2021; Schrader et al., 2013, 2014; Tenner et al., 2015; Miller et al., 2017; Siron et al., 2021, 2022).

Table 1. Major and minor element compositions of Wild 2 fragments determined by TEM-EDS and EPMA in this study

Track	Type	Fragment	Size (μm)	Depth (μm)	Target	Composition	SiO_2	TiO_2	Al_2O_3	Cr_2O_3	FeO	MnO	MgO	CaO	P_2O_5	Na2O	Total
T77	B	F7	4 × 3	Surface	Ol	Fo_{60}	33.5	–	0.58	0.04	35.3	0.74	29.6	0.20	–	–	100.0
T149	B	I/F11a	5 × 3	Surface	Ol	Fo_{85}	40.6	–	–	0.21	13.7	0.28	45.0	0.21	–	–	100.0
		I/F11b	2 × 2	Surface	Ol											–	
T172	B	F100	5 × 5	Surface	Lpx	$En_{95.9}Wo_{2.8}$	58.3	–	0.61	0.21	0.91	1.33	36.2	1.46	–	–	100.0
T191	B	B1/F1	4 × 3	Surface	Lpx	$En_{94}Wo_{0.7}$	59.6	–	0.22	1.17	3.11	1.20	34.4	0.35	–	–	100.0
T191	B	B1/F2	4 × 2	Surface	Ol	Fo_{98}	43.5	–	0.62	0.75	1.88	0.34	52.9	–	–	–	100.0
T191	B	B1/F3	3 × 3	Surface	Ol	$Fo_{98.4}$	40.7	–	–	0.51	1.63	0.26	56.9	–	–	–	100.0
T191	B	B1/F6	2 × 2	Surface	Ol	Fo_{75}	38.2	–	–	–	23.0	0.60	38.0	0.11	–	–	100.0
T220	B	TP10b/F10	4 × 2	Surface	Lpx	$En_{95.1}Wo_{3.4}$	59.4	0.19	2.86	0.81	0.94	0.56	33.6	1.66	–	–	100.0
				Surface	Ol	$Fo_{86.6}$	40.5	–	–	0.30	12.2	2.52	44.3	0.17	–	–	100.0
T220	B	TP10b/F11*	3.0 × 2.3	2.3	Lpx	$En_{96}Wo_3$	54.2	0.09	1.34	0.88	1.32	0.45	35.0	1.78	–	0.85	95.9
T220	B	TP10b/F12*	2.2 × 2.0	2.8	Lpx	$En_{94}Wo_{1.5}$	51.3	0.09	0.40	1.13	2.52	0.76	30.0	0.58	–	0.57	88.2
T220	B	TP10a/F3*	3.0 × 1.5	7.8	Ol	Fo_{68}	37.0	–	0.15	0.14	26.0	0.52	31.1	0.36	–	0.21	95.5
T220	B	TP10a/F4*	2.5 × 1.8	4.5	Lpx	$En_{84}Wo_5$	51.4	0.56	4.00	1.28	6.01	1.48	25.7	2.06	–	0.34	92.9
T220	B	TP10a/F5*	1.8 × 1.8	2.3	Lpx	$En_{80}Wo_{1.2}$	35.4	0.09	0.41	0.61	10.1	1.61	23.9	0.51	–	0.18	73.7
T22	A	F8	7 × 2	Surface	Ol	Fo_{86}	40.0	–	–	–	13.6	0.60	45.5	0.37	–	–	100.0
T22	A	F10	5 × 4	Surface	Ol	Fo_{71}	38.8	–	–	–	25.5	0.63	34.3	0.42	0.32	–	100.0
T22	A	F12	6 × 3	Surface	Ol	Fo_{82}	36.8	–	–	–	16.9	0.63	44.8	0.29	0.56	–	100.0
T175	A	F1	4 × 2	Surface	Ol	$Fo_{99.8}$	41.2	–	–	–	0.20	0.10	58.5	–	–	–	100.0

*Fragments exposed by SIMS Kohler beam and analyzed by an FE-PMA (12 kV, 500 pA). Due to the low electron beam current, MnO, TiO_2, and Na_2O contents were overdetermined, and MnO was corrected using functions derived from a number of olivine and pyroxene standards with known compositions, while the TiO_2 and Na_2O contents were uncorrected due to lack of standards with varying compositions. Other fragments were exposed by ultramicrotomy, and their major and minor element compositions were determined from their microtome slices using EDS installed on TEM, which were quantified using an EDAX Genesis analysis system by the k-factor element ratio technique (Cliff and Lorimer, 1975). Fragments T22/F8, F10, and F12 are chondrule-like fragments of olivine and glassy mesostasis. Fragment T220/TP10b/F10 comprises low-Ca pyroxene with an olivine inclusion.

Table 2. Oxygen isotope ratios of 16 Wild 2 fragments determined in this study

Track	Fragment	Mineral	Mg#	Cycle	$\delta^{18}O$	2σ	$\delta^{17}O$	2σ	$\Delta^{17}O$	2σ
T77	F7	Ol	60.0	10	5.1	1.8	5.6	2.4	3.0	2.5
T149	I/F11a	Ol	85.0	20	2.5	1.2	0.4	2.7	-1.0	2.3
T149	I/F11b	Ol	85.0	20	0.5	1.2	0.3	2.7	0.0	2.3
T172	F100	Lpx	98.6	20	-3.1	1.7	-5.9	3.3	-4.3	2.9
T191	B1/F1	Lpx	94.7	20	-2.0	1.6	-3.5	2.6	-2.4	2.3
T191	B1/F2	Ol	98.0	20	-1.9	2.1	-2.8	2.8	-1.8	2.0
T191	B1/F3	Ol	98.4	20	-0.7	2.4	-1.9	2.0	-1.6	1.5
T191	B1/F6	Ol	75.0	16	4.5	2.1	4.2	2.5	1.9	1.8
T220	TP10b/F10	Lpx	98.4	20	3.5	0.8	0.6	1.8	-1.3	1.7
T220	TP10b/F11*	Lpx	99.0	20	2.7	2.8	-1.0	2.3	-2.4	3.1
T220	TP10a/F3*	Ol	68.0	20	2.9	1.6	3.1	2.6	1.6	2.7
T220	TP10a/F4*	Lpx	88.4	20	4.7	1.6	1.1	2.6	-1.3	2.7
T22	F8	Ol	86.0	20	6.9	2.4	6.7	4.0	3.1	2.9
T22	F10	Ol	71.0	20	1.6	1.9	3.2	2.4	2.3	1.9
T22	F12	Ol	82.0	17	5.5	2.0	5.4	3.0	2.5	2.2
T175	F1	Ol	99.8	20	-50.4	2.4	-49.5	2.4	-23.3	1.4

*Fragments exposed by a 22×22 um SIMS Kohler beam and analyzed using a 1.5×1.0 um Gaussian beam; Others were analyzed using a typical 2.0 ×1.5 um Gaussian beam. Each fragment was analyzed once. The total cycle for each analysis is 20.